Journal of Computational Physics 562 (2026) 115036

Contents lists available at ScienceDirect

Journal of Computational Physics

journal homepage: www.elsevier.com/locate/jcp

Thermodynamically consistent modeling and energy-stable LDG schemes for semi-permeable interface flows

Ruihan Guo [a], Jie Shen [b], Shixin Xu [c,*], Xianmin Xu [d]

[a] School of Mathematics and Statistics, Zhengzhou University, Zhengzhou, 450001, China
[b] School of Mathematical Science, Eastern Institute of Technology, Ningbo, 315200, China
[c] Zu Chongzhi Center, Duke Kunshan University, 8 Duke Ave, Kunshan, Jiangsu, 215316, China
[d] State Key Laboratory of Mathematical Sciences, Academy of Mathematics and Systems Science, Chinese Academy of Sciences, Beijing, 100190, China

ARTICLE INFO

2000 MSC:
65M60
65H10
76T06
92C10

Keywords:
Energy stable scheme
Local discontinuous galerkin
Phase field method
Semi-permeable interface
Permeating Cahn-Hilliard-Navier-Stokes

ABSTRACT

We develop a thermodynamically consistent phase-field framework, *permeating CHNS (pCHNS)*, for solvent transport across semi-permeable interfaces driven by osmotic and hydrostatic pressure differences. The model establishes a *bidirectional coupling*: the fluid advects solute, while solute gradients regulate cross-interface solvent flux via osmotic pressure. An energy-variational derivation yields a closed energy-dissipation law, which we leverage to construct *fully discrete, energy-stable, high-order* algorithms: LDG spatial discretization, a decoupled first-order scheme with *unconditional energy stability*, and a semi-implicit spectral deferred correction (SDC) upgrade for high-order temporal accuracy while preserving dissipation. A *sharp-interface asymptotic analysis* shows that, under natural scalings, the diffuse model converges to a sharp-interface problem with the expected kinematic law, normal-stress jump, and solute impermeability conditions, thereby establishing diffuse-to-sharp consistency. Numerically, a space-time convergence study confirms design orders and energy decay; a 1D no-flow calibration demonstrates quantitative convergence to the sharp-interface prediction as the interface thickness vanishes; and 2D simulations examine how permeability, solute load, and shear shape droplet evolution and equilibrium morphology. The contributions are methodological and analytical, providing a robust computational framework for coupled fluid-interface-transport problems.

1. Introduction

Semi-permeable interfaces play a central role in both biological and industrial systems by regulating the selective transport of water and solutes across compartments [1,2]. In living cells, the plasma membrane is typically permeable to water but impermeable to most solutes, enabling essential physiological functions such as hydration, nutrient uptake, and waste removal [3,4]. As shown in Fig. 1(a), water exchange across a semi-permeable interface is controlled by the competition between osmotic pressure (generated by a jump in solute concentration) and hydrostatic pressure (arising from fluid stresses). Together, these forces determine the magnitude and direction of cross-interface flow, and their imbalance can cause pathological responses such as cell swelling or shrinkage, impairing cellular function [5]. Beyond biology, semi-permeable interfaces are the working principle behind industrial processes such as desalination, water purification, and chemical separation, as well as in membrane-based energy systems like fuel cells and batteries. In these contexts, the ability to control solvent flux, maintain mechanical integrity, and predict interfacial behavior under large

* Corresponding author.
E-mail address: shixin.xu@dukekunshan.edu.cn (S. Xu).

https://doi.org/10.1016/j.jcp.2026.115036
Received 29 October 2025; Received in revised form 10 April 2026; Accepted 11 May 2026
Available online 14 May 2026

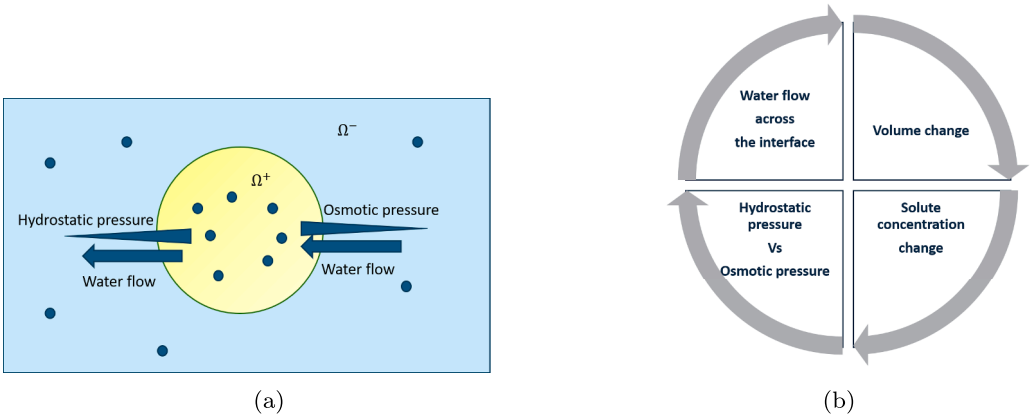

Fig. 1. Schematic of semi-permeable interface dynamics. (a) Domain and pressure illustration; (b) Semi-permeable interface feedback process. Water permeates across the interface in response to an imbalance between hydrostatic and osmotic pressures. This permeation changes the droplet volume; because solute cannot cross the interface, its inside/outside concentrations adjust accordingly, which in turn modifies the osmotic pressure. The droplet evolves until the osmotic and hydrostatic contributions balance, yielding an equilibrium size and shape.

osmotic or pressure gradients is critical for performance and design. Accurate modeling of semi-permeable interfaces is therefore vital for understanding fundamental biological processes and optimizing advanced engineering applications.

Modeling fluid transport across semi-permeable interfaces driven simultaneously by osmotic and hydrostatic pressures is challenging. Classical sharp-interface formulations, such as immersed boundary methods [6–8], treat the interface as an explicitly tracked moving boundary. Building on this paradigm, Yao and Mori developed an immersed-boundary model that couples fluid motion, interface mechanics, and solute transport [9]. While these approaches capture basic interfacial phenomena, they demand the specification and numerical enforcement of delicate jump conditions for velocity, stress, and selectively permeable fluxes, and they are prone to difficulties under large deformations, near contact, or topological change.

Phase-field methods provide a robust alternative by representing membranes as diffuse interfaces through continuous order parameters, naturally accommodating topological changes and large deformations. They have been successfully applied to vesicle dynamics, droplet interactions, and fluid–structure coupling problems [10–15]. However, osmotic-pressure-driven interfacial water flow remains relatively unexplored. Recent extensions have begun to address this gap. Rätz [16] derived a thermodynamically consistent phase-field approximation that converges to a sharp-interface limit, but the model only accounts for solute concentration. Tang et al. [4] developed a dynamic phase-field model for vesicle growth or shrinkage driven by osmotic pressure, in which interior and exterior osmotic free-energy contributions are incorporated to describe deformation dynamics and equilibrium morphology. Their framework, however, does not explicitly couple solute evolution with fluid motion. In the present work, our formulation is closer in spirit to the thermodynamically consistent diffuse-interface framework of Garcke et al. [17], where phase-dependent quantities are coupled through an energy-dissipation structure and related systematically to a sharp-interface description. In particular, rather than prescribing growth or shrinkage through target interior/exterior states, we consider a semi-permeable interface model in which the direction of solvent transport and the resulting swelling or shrinkage emerge dynamically from the competition between osmotic and hydrostatic/mechanical effects near the interface. These studies motivate the need for a more comprehensive framework that integrates fluid motion, solute transport, and interfacial water flow in a thermodynamically consistent setting.

The Cahn-Hilliard-Navier-Stokes (CHNS) system offers a natural setting for modeling fluid-interface interactions, particularly in two-phase flow systems. However, extending it to handle semi-permeable interfaces, where water can independently traverse the interface due to osmotic pressure, poses new challenges. Specifically, it is nontrivial to capture the strong coupling between solute concentration, osmotic pressure, and interfacial transport flow within a diffuse-interface framework. Several prior efforts have addressed related challenges: Camley et al. [18] modeled intracellular confinement of active substances, Lowengrub et al. [19] introduced phase-field models with inextensibility constraints, and Garcke et al. [17] proposed models for surfactants soluble in both phases but constrained at interfaces. However, these models do not account for osmotic-driven transport across semi-permeable interfaces.

The primary objective of this work is to develop a thermodynamically consistent phase-field model that accounts for water transport across semi-permeable interfaces driven by osmotic pressure differences. Our formulation extends the CHNS system to incorporate fluid-structure coupling and membrane permeability while preserving energy stability, thereby providing a more realistic framework for simulating interfacial fluid transport in biological and industrial settings.

The energy variational approach [13,20,21] leads to a highly nonlinear, coupled permeating Cahn-Hilliard-Navier-Stokes (pCHNS) system, where an Allen-Cahn term captures the volume change induced by the interfacial water flow. Simulating this system poses significant challenges due to its strong nonlinear couplings. Although many numerical schemes have been developed for Allen-Cahn or Cahn-Hilliard-Navier-Stokes systems [22–29], our model exhibits a more intricate feedback structure: convection drives solute transport, the resulting solute gradient generates osmotic pressure, and osmotic flux in turn leads to volume changes that affect solute

concentration as shown in Fig. 1 b. Consequently, the interplay between fluid motion, interfacial dynamics, and solute distribution is significantly stronger and more nonlinear than in traditional models.

The second goal of this work is to develop energy-stable and decoupled numerical schemes for the proposed system. For spatial discretization, we adopt the local discontinuous Galerkin (LDG) method [30,31], which provides high-order accuracy, nonlinear stability, and adaptability to arbitrary mesh refinement (h- and p-adaptivity). For time integration, we first construct a first-order decoupled scheme and rigorously prove its energy stability under the LDG framework. Although efficient, this scheme is limited to first-order temporal accuracy. To address this, we incorporate the semi-implicit spectral deferred correction (SDC) method [32,33], enabling high-order accuracy in both space and time for the thermodynamically consistent phase-field model of fluid transport through semi-permeable interfaces.

This paper is organized as follows. In Section 2, we propose the phase-field model for semi-permeable interfaces. In Section 3, the sharp interface limit of the proposed model is presented by asymptotic analysis. Section 4 presents the numerical schemes: Section 4.1 introduces the first-order decoupled temporal scheme, Section 4.2 describes the LDG method for spatial discretization and proves its energy stability, and Section 4.3 applies the semi-implicit SDC method to enhance temporal accuracy. Section 5 provides numerical results validating the theoretical analysis and exploring the effects of interface permeability and osmotic pressure. Finally, concluding remarks are given in Section 6.

2. Mathematical model

For simplicity, we consider the semi-permeable interfaces with constant surface tension. We start with the following conservation laws [13]

$$\begin{cases} \rho\left(\frac{\partial \boldsymbol{u}}{\partial t} + (\boldsymbol{u}\cdot\nabla)\boldsymbol{u}\right) = \nabla\cdot\boldsymbol{\sigma}_\eta + \nabla\cdot\boldsymbol{\sigma}_\phi, & \text{in } \Omega, \\ \nabla\cdot\boldsymbol{u} = 0, & \text{in } \Omega, \\ \frac{\partial}{\partial t}(\zeta_\pm C_\pm) + \nabla\cdot(\zeta_\pm C_\pm \boldsymbol{u}) = -\nabla\cdot(\zeta_\pm \boldsymbol{J}_\pm), & \text{in } \Omega, \\ \frac{\partial \phi}{\partial t} + \nabla\cdot(\phi\boldsymbol{u}) = -\nabla\cdot\boldsymbol{J}_\phi + S_\phi|\nabla\phi|, & \text{in } \Omega, \end{cases} \tag{1}$$

where ρ is the density, $C_\pm$ is the concentration inside/outside of the droplet, $\boldsymbol{u}$ is the velocity and ϕ is the label function and $\zeta_+(\phi)$ is a smooth index function given by Garcke et al. [17]

$$\zeta_+(\phi) = \begin{cases} 1 & \phi \geq 1, \\ \frac{1}{2}(1+\frac{1}{2}\phi(3-\phi^2)) & |\phi|<1, \\ 0 & \phi \leq -1, \end{cases} \quad \zeta_-(\phi) = 1-\zeta_+(\phi).$$

Here, the first equation represents the conservation of momentum, involving two unknown stresses $\boldsymbol{\sigma}_\eta$ and $\boldsymbol{\sigma}_\phi$. The second equation enforces fluid incompressibility, the third describes the conservation of solute with unknown fluxes $\boldsymbol{J}_\pm$, and the last is a Cahn-Hilliard-type equation that tracks interface evolution with flux $\boldsymbol{J}_\phi$ and a source term S_ϕ arising from interfacial water transport. The latter is localized near the membrane by a smooth delta function $|\nabla\phi|$ as in Li et al. [34].

The total energy consists of kinetic, entropy and phase-mixing energy

$$\begin{aligned} E =& E_{kin} + E_{entropy} + E_{mix} \\ =& \int_\Omega \rho\frac{|\boldsymbol{u}|^2}{2}d\boldsymbol{x} + \int_\Omega RT\left(\zeta_+ C_+(\ln\frac{C_+}{c_\infty}-1) + \zeta_- C_-(\ln\frac{C_-}{c_\infty}-1)\right)d\boldsymbol{x} + \int_\Omega \lambda\left(\frac{l|\nabla\phi|^2}{2} + \frac{F(\phi)}{l}\right)d\boldsymbol{x}, \end{aligned} \tag{2}$$

where R is the universal ideal gas constant, T is temperature, c_∞ is the characteristic concentration, ρ is density, λ is surface energy density, l is surface thickness and $F(\phi) = \frac{1}{4}(\phi^2-1)^2$ is the double-well potential.

Corresponding to the total energy, we could define the chemical potential of ϕ

$$\tilde{\mu}_\phi = \lambda(-l\Delta\phi + \frac{1}{l}F'(\phi)) - RT\left(\frac{\partial\zeta_+}{\partial\phi}C_+ + \frac{\partial\zeta_-}{\partial\phi}C_-\right),$$

and the chemical potential of solutes inside/outside of the droplet

$$\mu_c^\pm = RT\ln\frac{C_\pm}{c_\infty}.$$

The dissipative functional consists of fluid friction, irreversible mixing of the substance and two phases in the bulk, and interfacial transport friction.

$$\Delta = \int_\Omega \left(2\eta|D_\eta|^2 + \sum_\pm \zeta_\pm\frac{D_\pm C_\pm}{RT}|\nabla\mu_c^\pm|^2 + \mathcal{M}|\nabla\tilde{\mu}_\phi|^2 + K|\nabla\phi||\tilde{\mu}_\phi|^2\right)d\boldsymbol{x}, \tag{3}$$

where η is the viscosity of the fluid, $D_\eta = \frac{1}{2}(\nabla\boldsymbol{u} + (\nabla\boldsymbol{u})^T)$ is the strain rate, $\mathcal{M}$ is the phenomenological mobility, $D_\pm$ is the intrinsic diffusion coefficient of substance in $\Omega^\pm$, K is the interface permeability.

The energy dissipative law [20,21,35] states that without external force acting on the system, the changing rate of total energy equals to the dissipation

$$\frac{dE}{dt} = \frac{dE_{kin}}{dt} + \frac{dE_{entropy}}{dt} + \frac{dE_{mix}}{dt} = -\Delta.$$

Using the definition of the total energy functional (2) and the conservation laws in (1), we can obtain the following energy dissipation relation (see Appendix for a detailed derivation):

$$\frac{dE}{dt} = -\int_\Omega \nabla \boldsymbol{u} : (\boldsymbol{\sigma}_\eta + \boldsymbol{\sigma}_\phi)\, d\boldsymbol{x} - \int_\Omega p\nabla\cdot\boldsymbol{u}\, d\boldsymbol{x} - \int_\Omega \lambda l^2(\nabla\phi\otimes\nabla\phi) : \nabla\boldsymbol{u}\, d\boldsymbol{x} + \int_\Omega \left(\zeta_+\boldsymbol{J}_+\cdot\nabla\mu_c^+ + \zeta_-\boldsymbol{J}_-\cdot\nabla\mu_c^-\right) d\boldsymbol{x} + \int_\Omega \boldsymbol{J}_\phi\cdot\nabla\tilde{\mu}_\phi\, d\boldsymbol{x} + \int_\Omega \tilde{\mu}_\phi S_\phi|\nabla\phi|\, d\boldsymbol{x}.$$

By comparing the terms above with the dissipation functional given in Eq. (3), we can identify the explicit expressions for the unknown quantities such as the fluxes and stress tensors

$$\boldsymbol{J}_\phi = -\mathcal{M}\nabla\tilde{\mu}_\phi,\quad \boldsymbol{J}_\pm = -\frac{D_\pm C_\pm}{RT}\nabla\mu_c^\pm = -D_\pm\nabla C_\pm,$$
$$\boldsymbol{\sigma}_\eta = 2\eta D_\eta - p\mathbf{I},\quad \boldsymbol{\sigma}_\phi = -\lambda l^2(\nabla\phi\otimes\nabla\phi),\quad S_\phi = -K\tilde{\mu}_\phi.$$

Substituting the above into (1) yields the phase-field model for the semi-permeable interface

$$\frac{\mathbf{D}\phi}{\mathbf{D}t} = \nabla\cdot(\mathcal{M}\nabla\tilde{\mu}_\phi) - K\tilde{\mu}_\phi|\nabla\phi|,$$
$$\frac{\mathbf{D}}{\mathbf{D}t}(\zeta_\pm C_\pm) = \nabla\cdot(\zeta_\pm D_\pm\nabla C_\pm),$$
$$\rho\frac{\mathbf{D}\boldsymbol{u}}{\mathbf{D}t} = \nabla\cdot(\eta(\nabla\boldsymbol{u} + (\nabla\boldsymbol{u})^T)) - \nabla p - \lambda l^2(\nabla\phi\otimes\nabla\phi)),$$
$$\nabla\cdot\boldsymbol{u} = 0,$$
$$\tilde{\mu}_\phi = \lambda(-l\Delta\phi + F'(\phi)) - RT\left(\frac{\partial\zeta_+}{\partial\phi}C_+ + \frac{\partial\zeta_-}{\partial\phi}C_-\right),$$

with boundary conditions

$$\nabla\phi\cdot\boldsymbol{n}|_{\partial\Omega} = 0,\quad \nabla C_\pm\cdot\boldsymbol{n}|_{\partial\Omega} = 0,\quad \nabla\tilde{\mu}_\phi\cdot\boldsymbol{n}|_{\partial\Omega} = 0,\quad \boldsymbol{u}|_{\partial\Omega} = 0.$$

Remark 2.1 (Toward more realistic membranes: bending and surface-area control)**.** In this work we deliberately isolate the role of *interface permeability* in osmotic-driven transport. More complete cell-membrane physics, such as curvature elasticity (Helfrich bending), inextensibility/surface-area control, and variable surface tension can be incorporated in a thermodynamically consistent way by augmenting the free energy with higher-order terms; see, e.g., Shen et al. [13], Du et al. [36]. These extensions enrich the framework to capture curvature-dependent mechanics and shape transitions. Below, we outline a representative extension of the pCHNS model with bending and surface area control; a detailed numerical study will be reported in future work. Define

$$G(\phi) = \frac{l}{2}|\nabla\phi|^2 + \frac{(1-\phi^2)^2}{4l},\qquad f(\phi) = \frac{\delta G}{\delta\phi} = -l\Delta\phi + \frac{1}{l}(\phi^2-1)\phi,$$

and the diffuse interfacial area

$$S(\phi) = \int_\Omega G(\phi)\, d\boldsymbol{x},$$

with $S(\phi_0)$ a prescribed target. A bending contribution yields the auxiliary field

$$g(\phi) = -l\Delta f(\phi) + \frac{1}{l}(3\phi^2-1)\, f(\phi),$$

which is the variational derivative of the classical Helfrich-type bending energy in the phase-field setting.

The solvent-solute-interface system then reads

$$\frac{\boldsymbol{D}\phi}{\boldsymbol{D}t} = \nabla\cdot\left(\mathcal{M}\,\nabla\tilde{\mu}_\phi\right) - K\,\tilde{\mu}_\phi\,|\nabla\phi|,$$
$$\frac{\boldsymbol{D}}{\boldsymbol{D}t}\left(\zeta_\pm C_\pm\right) = \nabla\cdot\left(\zeta_\pm D_\pm\,\nabla C_\pm\right),$$
$$\rho\,\frac{\boldsymbol{D}\boldsymbol{u}}{\boldsymbol{D}t} = \nabla\cdot\left(\eta(\nabla\boldsymbol{u} + (\nabla\boldsymbol{u})^T)\right) - \nabla p - \lambda l(\nabla\phi\otimes\nabla\phi),$$
$$\nabla\cdot\boldsymbol{u} = 0,$$
$$\tilde{\mu}_\phi = \frac{\hat{\kappa}_B}{l^2}\,g(\phi) \;+\; \mathcal{M}_s\,\frac{S(\phi)-S(\phi_0)}{S(\phi_0)}\,f(\phi) \;-\; RT\left(\zeta_+'(\phi)\,C_+ + \zeta_-'(\phi)\,C_-\right).$$

Here $\hat{\kappa}_B$ is a (nondimensional) bending modulus, and $\mathcal{M}_s$ penalizes deviation of $S(\phi)$ from the prescribed $S(\phi_0)$, modeling global inextensibility. This extension preserves the energetic structure: the added contributions enter only through $\tilde{\mu}_\phi$ as variational derivatives of bending and area-penalty energies, so the same energy-dissipation law holds under the usual no-flux/periodic boundary conditions. The purpose of this remark is only to illustrate the flexibility of the present energetic formulation and to indicate a possible direction for future extension. These additional ingredients are not used in the sharp-interface analysis, numerical scheme design, or simulations presented in the remainder of this paper.

The Allen–Cahn-type source term $-K\tilde{\mu}_\phi|\nabla\phi|$ represents a phenomenological solvent flux localized near the semi-permeable interface, where K plays the role of an effective membrane hydraulic permeability. Its sign is determined by the generalized interfacial chemical potential $\tilde{\mu}_\phi$, which contains both capillary/hydrostatic and osmotic contributions. Consequently, the membrane may either expel water or admit water, depending on the competition between these two effects. This is also consistent with the sharp-interface limit derived in Section 3, where the normal transmembrane velocity is driven jointly by the normal stress jump and the concentration jump across the interface. Therefore, the model does not predict shrinkage only; rather, it allows both shrinkage and swelling, with the direction of solvent transport determined by the instantaneous osmotic–hydrostatic imbalance.

Let L^*, U^*, $C^* = c_\infty$, and D^* denote the characteristic length, velocity, concentration, and diffusion coefficient, respectively. Define the characteristic time and chemical potential as $t^* = \frac{L^*}{U^*}$ and $\mu^* = \frac{\lambda}{L^*}$. Using these scalings, the dimensionless form of the system is given by:

$$
\begin{aligned}
&\frac{\mathbf{D}\phi}{\mathbf{D}t} = \nabla\cdot(\mathcal{M}\nabla\tilde{\mu}_\phi) - \frac{K}{Ca}\tilde{\mu}_\phi|\nabla\phi|,\\
&\frac{\mathbf{D}}{\mathbf{D}t}(\zeta_\pm C_\pm) = \frac{1}{Pe}\nabla\cdot(\zeta_\pm D_\pm\nabla C_\pm),\\
&Re\frac{\mathbf{D}\boldsymbol{u}}{\mathbf{D}t} = \nabla\cdot(\eta(\nabla\boldsymbol{u}+(\nabla\boldsymbol{u})^T)) - \nabla p - \frac{\epsilon}{Ca}\nabla\cdot(\nabla\phi\otimes\nabla\phi),\\
&\nabla\cdot\boldsymbol{u} = 0,\\
&\tilde{\mu}_\phi = -\epsilon\Delta\phi + \frac{1}{\epsilon}F'(\phi) - \beta\left(\frac{\partial\zeta_+}{\partial\phi}C_+ + \frac{\partial\zeta_-}{\partial\phi}C_-\right),
\end{aligned}
$$

where

$$
Re = \frac{\rho U^*L^*}{\eta^*}, Pe = \frac{U^*L^*}{D^*}, Ca = \frac{\eta^*U^*}{\lambda}, \beta = \frac{RTC^*L}{\lambda}, K = \frac{K\eta^*}{L^*},\ \epsilon = \frac{l}{L^*}.
$$

Using the fact that

$$
\begin{aligned}
-\epsilon\nabla\cdot(\nabla\phi\otimes\nabla\phi) &= -\epsilon\nabla\phi\Delta\phi - \frac{\epsilon}{2}\nabla|\nabla\phi|^2\\
&= \tilde{\mu}_\phi\nabla\phi + \beta(C_+\nabla\zeta_+ + C_-\nabla\zeta_-) - \nabla(\frac{1}{\epsilon}F(\phi) + \frac{\epsilon}{2}|\nabla\phi|^2),
\end{aligned}
$$

the above system could be written as

$$
\frac{\partial\phi}{\partial t} + \boldsymbol{u}\cdot\nabla\phi = \nabla\cdot(\mathcal{M}\nabla\tilde{\mu}_\phi) - \frac{K}{Ca}\tilde{\mu}_\phi|\nabla\phi|, \tag{4a}
$$

$$
\frac{\partial(\zeta_\pm C_\pm)}{\partial t} + \nabla\cdot(\boldsymbol{u}\zeta_\pm C_\pm) = \frac{1}{Pe}\nabla\cdot(\zeta_\pm D_\pm\nabla C_\pm), \tag{4b}
$$

$$
Re\left(\frac{\partial\boldsymbol{u}}{\partial t} + (\boldsymbol{u}\cdot\nabla)\boldsymbol{u}\right) = \nabla\cdot(\eta(\nabla\boldsymbol{u}+(\nabla\boldsymbol{u})^T)) - \nabla p + \frac{1}{Ca}\tilde{\mu}_\phi\nabla\phi + \frac{\beta}{Ca}(C_+\nabla\zeta_+ + C_-\nabla\zeta_-), \tag{4c}
$$

$$
\nabla\cdot\boldsymbol{u} = 0, \tag{4d}
$$

$$
\tilde{\mu}_\phi = -\epsilon\Delta\phi + \frac{1}{\epsilon}F'(\phi) - \beta\left(\frac{\partial\zeta_+}{\partial\phi}C_+ + \frac{\partial\zeta_-}{\partial\phi}C_-\right) = \mu_\phi - \beta\left(\frac{\partial\zeta_+}{\partial\phi}C_+ + \frac{\partial\zeta_-}{\partial\phi}C_-\right), \tag{4e}
$$

with boundary conditions (2), where $\mu_\phi = -\epsilon\Delta\phi + \frac{1}{\epsilon}F'(\phi)$ is the standard chemical potential in phase filed method.

Theorem 2.1. *The above system (4) with boundary conditions (2) satisfies the following energy dissipation law*

$$
\begin{aligned}
&\frac{d}{dt}\left(\frac{Re}{2}\int_\Omega|\boldsymbol{u}|^2d\boldsymbol{x} + \frac{1}{Ca}\int_\Omega(\frac{\epsilon}{2}|\nabla\phi|^2 + \frac{1}{\epsilon}F(\phi))d\boldsymbol{x} + \sum_\pm\frac{\beta}{Ca}\int_\Omega\zeta_\pm C_\pm(\ln C_\pm - 1)d\boldsymbol{x}\right)\\
&= -\int_\Omega\eta|\nabla\boldsymbol{u}|^2d\boldsymbol{x} - \frac{1}{Ca}\int_\Omega\mathcal{M}|\nabla\tilde{\mu}_\phi|^2d\boldsymbol{x} - \frac{1}{Ca}\int_\Omega\frac{K}{Ca}|\tilde{\mu}_\phi|^2|\nabla\phi|d\boldsymbol{x} - \frac{\beta}{Ca}\frac{1}{Pe}\sum_\pm\int_\Omega\zeta_\pm D_\pm C_\pm|\nabla\mu_c^\pm|^2d\boldsymbol{x},
\end{aligned}
$$

where $\mu_c^\pm = \ln C_\pm$.

Proof. Multiplying Eq. (4a) by $\frac{\tilde{\mu}_\phi}{Ca}$ and integration by parts yields

$$
\frac{1}{Ca}\int_\Omega\frac{\partial\phi}{\partial t}\tilde{\mu}_\phi d\boldsymbol{x} + \frac{1}{Ca}\int_\Omega\boldsymbol{u}\cdot\nabla\phi\tilde{\mu}_\phi d\boldsymbol{x} = -\frac{1}{Ca}\int_\Omega\mathcal{M}|\nabla\tilde{\mu}_\phi|^2d\boldsymbol{x} - \frac{1}{Ca}\int_\Omega\frac{K}{Ca}|\tilde{\mu}_\phi|^2|\nabla\phi|d\boldsymbol{x}. \tag{5}
$$

Multiplying Eq. (4e) by $\frac{1}{Ca}\frac{\partial\phi}{\partial t}$ and integration by parts, we have

$$
\frac{1}{Ca}\int_\Omega\tilde{\mu}_\phi\frac{\partial\phi}{\partial t}d\boldsymbol{x} = \frac{1}{Ca}\frac{d}{dt}\int_\Omega(\frac{\epsilon}{2}|\nabla\phi|^2 + \frac{1}{\epsilon}F(\phi))d\boldsymbol{x} - \frac{\beta}{Ca}\int_\Omega\frac{\partial\phi}{\partial t}\left(\frac{\partial\zeta_+}{\partial\phi}C_+ + \frac{\partial\zeta_-}{\partial\phi}C_-\right)d\boldsymbol{x}. \tag{6}
$$

Then, the above two equations give

$$
\frac{1}{Ca}\frac{d}{dt}\int_\Omega(\frac{\epsilon}{2}|\nabla\phi|^2 + \frac{1}{\epsilon}F(\phi))d\boldsymbol{x} - \frac{\beta}{Ca}\int_\Omega\frac{\partial\phi}{\partial t}\left(\frac{\partial\zeta_+}{\partial\phi}C_+ + \frac{\partial\zeta_-}{\partial\phi}C_-\right)d\boldsymbol{x} + \frac{1}{Ca}\int_\Omega\boldsymbol{u}\cdot\nabla\phi\tilde{\mu}_\phi d\boldsymbol{x}
$$

Table 1
Summary of frequently used notation.

Notation	Meaning
ϕ	phase-field variable describing the interface location
$\zeta_+(\phi)$, $\zeta_-(\phi)$	smooth indicator functions for the two sides of the interface
C_+, C_-	solute concentrations in the interior and exterior regions
$\boldsymbol{u}$	fluid velocity
p	pressure
μ_ϕ	standard phase-field chemical potential, $\mu_\phi = -\epsilon\Delta\phi + \frac{1}{\epsilon}F'(\phi)$
$\tilde{\mu}_\phi$	generalized chemical potential including solute coupling
$\mu_c^\pm$	bulk solute chemical potentials, $\mu_c^\pm = \ln C_\pm$

$$= -\frac{1}{Ca}\int_\Omega \mathcal{M}|\nabla\tilde{\mu}_\phi|^2 d\boldsymbol{x} - \frac{1}{Ca}\int_\Omega \frac{K}{Ca}|\tilde{\mu}_\phi|^2|\nabla\phi| d\boldsymbol{x}. \tag{7}$$

For Eq. (4b), using the definition $\mu_c^\pm = \ln C_\pm$, it yields

$$\begin{aligned}
&\frac{\beta}{Ca}\int_\Omega \frac{\partial(\zeta_\pm C_\pm)}{\partial t}\mu_c^\pm d\boldsymbol{x} + \frac{\beta}{Ca}\int_\Omega \boldsymbol{u}\cdot\nabla(\zeta_\pm C_\pm)\mu_c^\pm d\boldsymbol{x}\\
=&\frac{\beta}{Ca}\int_\Omega \frac{\partial(\zeta_\pm C_\pm)}{\partial t}\mu_c^\pm d\boldsymbol{x} - \frac{\beta}{Ca}\int_\Omega \boldsymbol{u}\cdot(C_\pm\nabla\mu_c^\pm)\zeta_\pm d\boldsymbol{x}\\
=&\frac{\beta}{Ca}\int_\Omega \frac{\partial(\zeta_\pm C_\pm)}{\partial t}\mu_c^\pm d\boldsymbol{x} - \frac{\beta}{Ca}\int_\Omega \boldsymbol{u}\cdot\nabla C_\pm\zeta_\pm d\boldsymbol{x}\\
=&\frac{\beta}{Ca}\int_\Omega \frac{\partial(\zeta_\pm C_\pm)}{\partial t}\mu_c^\pm d\boldsymbol{x} + \frac{\beta}{Ca}\int_\Omega \boldsymbol{u}\cdot\nabla\zeta_\pm C_\pm d\boldsymbol{x}\\
=&-\frac{\beta}{Ca}\frac{1}{Pe}\int_\Omega \zeta_\pm D_\pm C_\pm|\nabla\mu_c^\pm|^2 d\boldsymbol{x}.
\end{aligned} \tag{8}$$

Multiplying Eq. (4c) with $\boldsymbol{u}$ and by the incompressibility constraint $\nabla\cdot\boldsymbol{u} = 0$, we have

$$\frac{d}{dt}\frac{Re}{2}\int_\Omega |\boldsymbol{u}|^2 d\boldsymbol{x} = -\int_\Omega \eta|\nabla\boldsymbol{u}|^2 d\boldsymbol{x} + \frac{1}{Ca}\int_\Omega \tilde{\mu}_\phi\nabla\phi\cdot\boldsymbol{u} d\boldsymbol{x} + \frac{\beta}{Ca}\int_\Omega (C_+\nabla\zeta_+ + C_-\nabla\zeta_-)\cdot\boldsymbol{u} d\boldsymbol{x}. \tag{9}$$

Adding the above three equations yields

$$\begin{aligned}
&\frac{d}{dt}\frac{Re}{2}\int_\Omega |\boldsymbol{u}|^2 d\boldsymbol{x} + \frac{d}{dt}\frac{1}{Ca}\int_\Omega (\frac{\epsilon}{2}|\nabla\phi|^2 + \frac{1}{\epsilon}F(\phi)) d\boldsymbol{x}\\
&-\frac{\beta}{Ca}\int_\Omega \frac{\partial\phi}{\partial t}\left(\frac{\partial\zeta_+}{\partial\phi}C_+ + \frac{\partial\zeta_-}{\partial\phi}C_-\right) d\boldsymbol{x} + \frac{\beta}{Ca}\int_\Omega \left(\frac{\partial(\zeta_+C_+)}{\partial t}\mu_c^+ + \frac{\partial(\zeta_-C_-)}{\partial t}\mu_c^-\right) d\boldsymbol{x}\\
=&\frac{d}{dt}\frac{Re}{2}\int_\Omega |\boldsymbol{u}|^2 d\boldsymbol{x} + \frac{d}{dt}\frac{1}{Ca}\int_\Omega (\frac{\epsilon}{2}|\nabla\phi|^2 + \frac{1}{\epsilon}F(\phi)) d\boldsymbol{x}\\
&+\frac{\beta}{Ca}\int_\Omega \left(\frac{\partial(\zeta_+C_+)}{\partial t}\mu_c^+ - \frac{\partial\zeta_+}{\partial t}C_+ + \frac{\partial(\zeta_-C_-)}{\partial t}\mu_c^- - \frac{\partial\zeta_-}{\partial t}C_-\right) d\boldsymbol{x}\\
=&\frac{d}{dt}\frac{Re}{2}\int_\Omega |\boldsymbol{u}|^2 dx + \frac{d}{dt}\frac{1}{Ca}\int_\Omega (\frac{\epsilon}{2}|\nabla\phi|^2 + \frac{1}{\epsilon}F(\phi)) d\boldsymbol{x}\\
&+\frac{d}{dt}\frac{\beta}{Ca}\int_\Omega (\zeta_+C_+(\ln C_+ - 1) + \zeta_-C_-(\ln C_- - 1)) d\boldsymbol{x}\\
=&-\int_\Omega \eta|\nabla\boldsymbol{u}|^2 d\boldsymbol{x} - \frac{1}{Ca}\int_\Omega \mathcal{M}|\nabla\tilde{\mu}_\phi|^2 d\boldsymbol{x} - \frac{1}{Ca}\int_\Omega \frac{K}{Ca}|\tilde{\mu}_\phi|^2|\nabla\phi| d\boldsymbol{x} - \frac{\beta}{Ca}\frac{1}{Pe}\sum_\pm\int_\Omega \zeta_\pm D_\pm C_\pm|\nabla\mu_c^\pm|^2 d\boldsymbol{x}.
\end{aligned}$$

□

For the reader's convenience, we briefly summarize several frequently used quantities (see Table 1).

3. Sharp interface limit

In this section we derive the sharp interface limit of (4) as the interfacial thickness $\epsilon \to 0$, following the matched asymptotics framework in Rätz [16], Xu et al. [37]. Hereinafter, we adopt the scalings $\mathcal{M} = M_0\epsilon$. We assume that there is an interface $\Gamma(t) = \{x|\phi(x,t) = 0\}$. The domain Ω is separated into two parts $\Omega^+(t) = \{x : \phi(x,t) > 0\}$ and $\Omega^-(t) = \{x : \phi(x,t) < 0\}$ by $\Gamma(t)$. We will analyze the sharp interface limit of the phase-field model (4) below. For simplicity in presentation, we assume all the physical coefficients are constant and rewrite the Eq. (4) as follows,

$$\frac{\partial\phi_\epsilon}{\partial t} + \boldsymbol{u}_\epsilon\cdot\nabla\phi_\epsilon = \epsilon M_0\Delta\mu_\epsilon - \frac{K}{Ca}\mu_\epsilon|\nabla\phi_\epsilon|, \tag{10a}$$

$$\frac{\partial(\zeta_{\pm}(\phi_\epsilon)C_{\pm,\epsilon})}{\partial t} + \nabla\cdot(\boldsymbol{u}_\epsilon\zeta_{\pm}(\phi_\epsilon)C_{\pm,\epsilon}) = \frac{D_{\pm}}{Pe}\nabla\cdot(\zeta_{\pm}(\phi_\epsilon)\nabla C_{\pm,\epsilon}), \tag{10b}$$

$$Re\left(\frac{\partial \boldsymbol{u}_\epsilon}{\partial t} + (\boldsymbol{u}_\epsilon\cdot\nabla)\boldsymbol{u}_\epsilon\right) = \eta\Delta\boldsymbol{u}_\epsilon - \nabla p_\epsilon + \frac{1}{Ca}\mu_\epsilon\nabla\phi_\epsilon + \frac{\beta}{Ca}(C_{+,\epsilon}-C_{-,\epsilon})\zeta'_{+}(\phi_\epsilon)\nabla\phi_\epsilon, \tag{10c}$$

$$\nabla\cdot\boldsymbol{u}_\epsilon = 0, \tag{10d}$$

$$\mu_\epsilon = -\epsilon\Delta\phi_\epsilon + \frac{1}{\epsilon}F'(\phi_\epsilon) - \beta\big(C_{+,\epsilon}-C_{-,\epsilon}\big)\zeta'_{+}(\phi_\epsilon), \tag{10e}$$

Here the dependence of the unknowns on the parameter ϵ are explicitly given. We have also used the fact that $\zeta'_{+}+\zeta'_{-}=0$.

Outer expansions: . Far from the two-phase interface, we use the following ansatz:

$$\begin{cases} \mu_\epsilon = \epsilon^{-1}\mu^{\pm}_{-1} + \mu^{\pm}_0 + \epsilon\mu^{\pm}_1 + \cdots, \\ \phi_\epsilon = \phi^{\pm}_0 + \epsilon\phi^{\pm}_1 + \cdots, \\ C_{\pm,\epsilon} = C^{\pm}_{\pm,0} + \epsilon C^{\pm}_{\pm,1} + \cdots, \\ \boldsymbol{u}_\epsilon = \boldsymbol{u}^{\pm}_0 + \epsilon\boldsymbol{u}^{\pm}_1 + \cdots, \\ p_\epsilon = p^{\pm}_0 + \epsilon p^{\pm}_1 + \cdots, \end{cases}$$

then the leading order of Eq. (10e) yields

$$\mu^{\pm}_{-1} = F'(\phi^{\pm}_0) = (\phi^{\pm}_0)^3 - \phi^{\pm}_0. \tag{11}$$

The leading order of the phase field Eq. (10a) and the momentum (10c) give

$$\mu^{\pm}_{-1}|\nabla\phi^{\pm}_0| = 0,\ \ \mu^{\pm}_{-1}\nabla\phi^{\pm}_0 = 0.$$

Combing with the Eq. (11), we have

$$\phi^{\pm}_0 = c^{\pm}_{const},$$

where $c^{\pm}_{const}$ are constants.

Then by using the fact that $\nabla\phi^{\pm}_0 = 0$, the next order of the Eq. (10c) is

$$Re\left(\frac{\partial \boldsymbol{u}^{\pm}_0}{\partial t} + (\boldsymbol{u}^{\pm}_0\cdot\nabla)\boldsymbol{u}^{\pm}_0\right) = \eta\triangle\boldsymbol{u}^{\pm}_0 - \nabla p^{\pm}_0. \tag{12}$$

Similarly, the leading order of concentration (10b) and incompressibility (10d) give

$$\frac{\partial(\zeta^{\pm}_{\pm,0}C^{\pm}_{\pm,0})}{\partial t} + \nabla\cdot(\boldsymbol{u}^{\pm}_0\zeta^{\pm}_{\pm,0}C^{\pm}_{\pm,0}) = \frac{D_{\pm}}{Pe}\nabla\cdot(\zeta^{\pm}_{\pm,0}\nabla C^{\pm}_{\pm,0}), \tag{13}$$

$$\nabla\cdot\boldsymbol{u}^{\pm}_0 = 0. \tag{14}$$

Inner expansions. We introduce the signed distance function $d(\boldsymbol{x})$ to the interface Γ, which is positive in Ω^+ and negative in Ω^-. Then the unit normal of the interface pointing to Ω^+ is given $\nabla d = \boldsymbol{\nu}$. After defining a new rescaled variable $\xi = \frac{d(\boldsymbol{x})}{\epsilon}$, for any scalar function $f(\boldsymbol{x})$, we can rewrite it as $f(\boldsymbol{x}) = \tilde{f}(\boldsymbol{x},\xi)$, and the relevant operators are

$$\begin{aligned} \nabla f(\boldsymbol{x}) &= \nabla_{\boldsymbol{x}}\tilde{f} + \epsilon^{-1}\partial_\xi\tilde{f}\boldsymbol{\nu}, \\ \nabla^2 f(\boldsymbol{x}) &= \nabla^2_{\boldsymbol{x}}\tilde{f} + \epsilon^{-1}\partial_\xi\tilde{f}\kappa + 2\epsilon^{-1}\big(\boldsymbol{\nu}\cdot\nabla_{\boldsymbol{x}}\big)\partial_\xi\tilde{f} + \epsilon^{-2}\partial_{\xi\xi}\tilde{f}, \\ \partial_t f &= \partial_t\tilde{f} + \epsilon^{-1}\partial_\xi\tilde{f}\partial_t d, \end{aligned}$$

where $\kappa = \nabla\cdot\boldsymbol{\nu}$ is the curvature of Γ.

In the inner region, we assume that

$$\begin{cases} \tilde{\boldsymbol{u}}_\epsilon = \tilde{\boldsymbol{u}}_0 + \epsilon\tilde{\boldsymbol{u}}_1 + \epsilon^2\tilde{\boldsymbol{u}}_2 + o\big(\epsilon^2\big), \\ \tilde{\phi}_\epsilon = \tilde{\phi}_0 + \epsilon\tilde{\phi}_1 + \epsilon^2\tilde{\phi}_2 + o\big(\epsilon^2\big), \\ \tilde{p}_\epsilon = \tilde{p}_0 + \epsilon\tilde{p}_1 + \epsilon^2\tilde{p}_2 + o\big(\epsilon^2\big), \\ \tilde{C}_{\epsilon,\pm} = \tilde{C}_{\pm,0} + \epsilon\tilde{C}_{\pm,1} + \epsilon^2\tilde{C}_{\pm,2} + o\big(\epsilon^2\big), \\ \tilde{\mu}_\epsilon = \epsilon^{-1}\tilde{\mu}_{-1} + \tilde{\mu}_0 + \epsilon\tilde{\mu}_1 + o(\epsilon). \end{cases}$$

The leading order of the Eqs. (10e) and (10a) gives

$$\tilde{\mu}_{-1} = \partial_{\xi\xi}\tilde{\phi}_0 + F'(\tilde{\phi}_0), \tag{16a}$$

$$\partial_{\xi\xi}\tilde{\mu}_{-1} - \frac{K}{Ca}\tilde{\mu}_{-1}|\partial_\xi\tilde{\phi}| = 0. \tag{16b}$$

The solvability condition of the above equations imply

$$\tilde{\mu}_{-1} = 0,\ \tilde{\phi}_0 = \tanh\frac{\xi}{\sqrt{2}}. \tag{17}$$

(One can easily verify that the above formula satisfies (16a) and (16b).) Then the matching condition $\lim_{\xi\to\pm\infty}\tilde{\phi}_0 = \phi_0^{\pm}$ yields

$$\phi_0^{\pm} = \pm 1,\ \mu_{-1}^{\pm} = 0.$$

Using this, the fluid and concentration equations in the bulk region (12)–(14) are reduced to the following form, in $\Omega^{\pm}$

$$\begin{cases} Re\left(\dfrac{\partial \boldsymbol{u}_0^{\pm}}{\partial t} + (\boldsymbol{u}_0^{\pm}\cdot\nabla)\boldsymbol{u}_0^{\pm}\right) = \eta\triangle\boldsymbol{u}_0^{\pm} - \nabla p_0^{\pm}, \\ \nabla\cdot\boldsymbol{u}_0^{\pm} = 0, \\ \dfrac{\partial C_{\pm,0}^{\pm}}{\partial t} + \nabla\cdot(\boldsymbol{u}_0^{\pm}C_{\pm,0}^{\pm}) = \dfrac{1}{Pe}\nabla\cdot(D_{\pm}\nabla C_{\pm,0}^{\pm}). \end{cases}$$

Here we have used that the fact that $\zeta_+(1) = 1-\zeta_-(1) = 1$ and $\zeta_+(-1) = 1-\zeta_-(-1) = 0$.

Then we can easily see that the leading order of Eq. (10c) is reduced to $\partial_{\xi\xi}\tilde{\boldsymbol{u}}_0 = 0$. Using a similar argument as in Xu et al. [37], we can derive $\tilde{\boldsymbol{u}}_0$ is independent of ξ. This further leads to the continuity of velocity across the interface

$$\boldsymbol{u}_0^{+} = \boldsymbol{u}_0^{-} = \tilde{\boldsymbol{u}}_0, \quad \text{and,} \quad [\boldsymbol{u}_0] = \boldsymbol{u}_0^{+} - \boldsymbol{u}_0^{-} = 0. \tag{18}$$

Hereinafter, we use $\boldsymbol{u}_0$ to represent the leading order of the velocity.

The leading order of the concentration Eq. (10b) yields

$$\partial_\xi(\zeta_{\pm}(\tilde{\phi}_0)\partial_\xi\tilde{C}_{\pm,0}) = 0.$$

This leads to $\tilde{C}_{\pm,0} = c_0 + c_1\int_{-\infty}^{\xi}\frac{1}{\zeta_{\pm}(\tilde{\phi}_0)}d\xi$, where c_0 and c_1 are constants independent of ξ. To ensure the boundedness of $\tilde{C}_{\pm,0}$, we need $c_1 = 0$. By the matching condition [16], this further implies

$$\partial_\xi\tilde{C}_{\pm,0} = 0,\ \tilde{C}_{\pm,0} = C_{\pm,0}.$$

Using the above facts, the next order of the Eqs. (10a) and (10e) are as follows

$$\partial_\xi\tilde{\phi}_0\partial_t d + \boldsymbol{\nu}\cdot\boldsymbol{u}_0\partial_\xi\tilde{\phi}_0 = M_0\partial_{\xi\xi}\tilde{\mu}_0 - \frac{K}{Ca}\tilde{\mu}_0\partial_\xi\tilde{\phi}_0, \tag{19a}$$

$$\tilde{\mu}_0 = \partial_{\xi\xi}\tilde{\phi}_1 - \partial_\xi\tilde{\phi}_0\kappa + F''(\tilde{\phi}_0)\tilde{\phi}_1 - \beta\zeta_+'(\tilde{\phi}_0)(C_{+,0}-C_{-,0}). \tag{19b}$$

Multiplying $\partial_\xi\tilde{\phi}_0$ with the Eq. (19b) and integration with respect to ξ in $(-\infty,\infty)$ gives

$$\int_{-\infty}^{\infty}\tilde{\mu}_0\partial_\xi\tilde{\phi}_0 d\xi = -\sigma\kappa - \beta(C_{+,0}-C_{-,0}),$$

with $\sigma = \int_{-\infty}^{\infty}(\partial_\xi\tilde{\phi}_0)^2 d\xi$. By integrating the Eq. (19a) with respect to ξ in $(-\infty,\infty)$, we have

$$2(\partial_t d + \boldsymbol{\nu}\cdot\boldsymbol{u}_0) = \frac{K}{Ca}(\sigma\kappa + \beta(C_{+,0}-C_{-,0})). \tag{20}$$

The ϵ^{-1} order of the Eq. (10c) gives

$$0 = -\partial_\xi\tilde{p}_0\boldsymbol{\nu} + \eta\partial_{\xi\xi}\tilde{\boldsymbol{u}}_1 + \frac{1}{Ca}\tilde{\mu}_0\partial_\xi\tilde{\phi}_0\boldsymbol{\nu} + \frac{\beta}{Ca}\zeta'(\tilde{\phi}_0)\partial_\xi\tilde{\phi}_0(C_{+,0}-C_{-,0})\boldsymbol{\nu}.$$

Integration the above equation with respect to ξ in $(-\infty,\infty)$ leads to

$$[-p_0\boldsymbol{\nu} + (\boldsymbol{\nu}\cdot\nabla)\boldsymbol{u}_0] = \frac{1}{Ca}(\sigma\kappa + \beta(C_{+,0}-C_{-,0}))\boldsymbol{\nu} - \frac{\beta}{Ca}(C_{+,0}-C_{-,0})\boldsymbol{\nu} = \frac{1}{Ca}\sigma\kappa\boldsymbol{\nu}. \tag{21}$$

Here we have used the matching condition that $\lim_{\xi\to\pm\infty}\tilde{p}_0 = p_0^{\pm}$ and $\lim_{\xi\to\pm\infty}(\partial_\xi\tilde{\boldsymbol{u}}_1) = \nu\cdot\nabla\boldsymbol{u}_0$. Combining Eqs. (20) and (21) yields the transmembrane velocity

$$\boldsymbol{u}_0\cdot\boldsymbol{\nu} - \boldsymbol{v}_0\cdot\boldsymbol{\nu} = \frac{K}{2}\left([-p_0\boldsymbol{\nu} + (\boldsymbol{\nu}\cdot\nabla)\boldsymbol{u}_0]\cdot\boldsymbol{\nu} + \frac{1}{Ca}\beta[C_0]\right). \tag{22}$$

Here $\boldsymbol{v}_0 = \frac{d\boldsymbol{x}}{dt}|_\Gamma$ is the velocity of the interface Γ.

For the concentration Eq. (10b), the ϵ^{-1} order is

$$\partial_\xi(\zeta_{\pm}(\tilde{\phi}_0))C_{\pm,0}\partial_t d + \partial_\xi(\zeta_{\pm}(\tilde{\phi}_0))\boldsymbol{\nu}C_{\pm,0}\cdot\boldsymbol{u}_0 = \frac{D_{\pm}}{Pe}(\boldsymbol{\nu}\cdot\partial_\xi(\zeta_{\pm}(\tilde{\phi}_0)\nabla C_{\pm,0}) + \partial_\xi((\zeta_{\pm}(\tilde{\phi}_0))\partial_\xi\tilde{C}_{1,\pm})).$$

Integration with respect to ξ in $(-\infty,\infty)$ and using the matching condition for $\tilde{C}_i^{\pm}$ and $\tilde{\phi}_i$ yield

$$C_{0,\pm}(\boldsymbol{u}_0 - \boldsymbol{v}_0)\cdot\boldsymbol{\nu} - \frac{D_{\pm}}{Pe}\boldsymbol{\nu}\cdot\nabla C_{\pm,0} = 0.$$

In summary, as ϵ approaching 0, the proposed model (4) converges to the following sharp interface model

$$\begin{cases} Re\left(\dfrac{\partial \boldsymbol{u}_0^{\pm}}{\partial t} + (\boldsymbol{u}_0^{\pm}\cdot\nabla)\boldsymbol{u}_0^{\pm}\right) = \eta \triangle \boldsymbol{u}_0^{\pm} - \nabla p_0^{\pm}, & \text{in } \Omega^{\pm} \\ \nabla\cdot\boldsymbol{u}_0^{\pm} = 0, & \text{in } \Omega^{\pm} \\ \dfrac{\partial C_{\pm,0}}{\partial t} + \nabla\cdot(\boldsymbol{u}_0^{\pm}C_{\pm,0}) = \dfrac{1}{Pe}\nabla\cdot(D_{\pm}\nabla C_{\pm,0}), & \text{in } \Omega^{\pm} \end{cases} \tag{23}$$

with interface condition on $\Gamma(t)$

$$\begin{cases} C_{\pm,0}(\boldsymbol{u}_0 - \boldsymbol{v}_0)\cdot\boldsymbol{\nu} - \dfrac{D_{\pm}}{Pe}\boldsymbol{\nu}\cdot\nabla C_{\pm,0} = 0, \\ \boldsymbol{u}_0\cdot\boldsymbol{\nu} - \boldsymbol{v}_0\cdot\boldsymbol{\nu} = \tilde{K}([-p_0\boldsymbol{\nu} + (\boldsymbol{\nu}\cdot\nabla)\boldsymbol{u}_0]\boldsymbol{\nu} + \beta Ca^{-1}[C_0]), \\ [-p_0\boldsymbol{\nu} + (\boldsymbol{\nu}\cdot\nabla)\boldsymbol{u}_0] = \dfrac{1}{Ca}\sigma\kappa\boldsymbol{\nu}, [\boldsymbol{u}_0] = 0, \\ \dfrac{d\boldsymbol{x}}{dt} = \boldsymbol{v}_0. \end{cases} \tag{24}$$

We set $\tilde{K} := K/2$ to absorb the factor coming from the normalization of the diffuse interfacial delta used in the phase field derivation. With this convention, the kinematic law takes the standard form used in the sharp-interface literature [38].

The sharp-interface law in the above interface condition (24) makes clear that the solvent flux across the membrane is bidirectional. Indeed, the normal relative velocity between the fluid and the interface is driven by the sum of two contributions: the hydrostatic/mechanical term associated with the normal stress jump and the osmotic term associated with the concentration jump. Hence, depending on their relative magnitudes and signs, the interface may move inward or outward, corresponding respectively to droplet shrinkage or swelling. In this sense, the permeability coefficient K controls the rate of transmembrane exchange, while the direction of the exchange is selected dynamically by the balance between osmotic and hydrostatic effects rather than by K alone.

4. Numerical scheme

The purpose of this section is to develop high-order, decoupled, and energy-stable numerical schemes to solve the model (4).

4.1. Semi-discrete scheme in time

A first-order and decoupled energy stable numerical scheme is as follows: assuming that $(\phi^n, \boldsymbol{u}^n, C_{\pm}^n)$ are already known, we then compute $(\phi^{n+1}, \boldsymbol{u}^{n+1}, C_{\pm}^{n+1})$ from the following temporal discrete system.

Step 1:

$$\begin{cases} \dfrac{\phi^{n+1}-\phi^n}{\Delta t} = \mathcal{M}\Delta\tilde{\mu}_{\phi}^{n+1} - \nabla\cdot(\phi^n\boldsymbol{u}_*^n) - \dfrac{K}{Ca}\tilde{\mu}_{\phi}^{n+1}|\nabla\phi^n|, \\ \tilde{\mu}_{\phi}^{n+1} = -\epsilon\Delta\phi^{n+1} + \dfrac{S}{\epsilon}(\phi^{n+1}-\phi^n) + \dfrac{1}{\epsilon}f(\phi^n) - \beta\displaystyle\sum_{\pm}\frac{\zeta_{\pm}^{n+1}-\zeta_{\pm}^n}{\phi^{n+1}-\phi^n}C_{\pm}^{n+1}, \\ \dfrac{\zeta_{\pm}^{n+1}C_{\pm}^{n+1} - \zeta_{\pm}^n C_{\pm}^n}{\Delta t} = \dfrac{1}{Pe}\nabla\cdot(\zeta_{\pm}^n D_{\pm}^n C_{\pm}^{n+1}\nabla\mu_{c_{\pm}}^{n+1}) - \nabla\cdot(\boldsymbol{u}_*^n\zeta_{\pm}^n C_{\pm}^n), \\ \mu_{c_{\pm}}^{n+1} = \ln C_{\pm}^{n+1}, \end{cases} \tag{25}$$

with

$$\boldsymbol{u}_*^n = \boldsymbol{u}^n - \frac{\Delta t}{CaRe}\phi^n\nabla\tilde{\mu}_{\phi}^{n+1} - \frac{\beta\Delta t}{CaRe}\sum_{\pm}\zeta_{\pm}^n C_{\pm}^n\nabla\mu_{c_{\pm}}^{n+1}. \tag{26}$$

Step 2:

$$Re\left(\frac{\widetilde{\boldsymbol{u}}^{n+1}-\boldsymbol{u}^n}{\Delta t} + (\boldsymbol{u}^n\cdot\nabla)\widetilde{\boldsymbol{u}}^{n+1}\right) = \eta\Delta\widetilde{\boldsymbol{u}}^{n+1} - \nabla p^n - \frac{1}{Ca}\phi^n\nabla\tilde{\mu}_{\phi}^{n+1} - \frac{\beta}{Ca}\sum_{\pm}\zeta_{\pm}^n C_{\pm}^n\nabla\mu_{c_{\pm}}^{n+1}. \tag{27}$$

Step 3:

$$\begin{cases} Re\dfrac{\boldsymbol{u}^{n+1}-\widetilde{\boldsymbol{u}}^{n+1}}{\Delta t} + \nabla(p^{n+1}-p^n) = 0, \\ \nabla\cdot\boldsymbol{u}^{n+1} = 0. \end{cases} \tag{28}$$

Taking the divergence of the first equation in (28) yields

$$-\Delta(p^{n+1}-p^n) = -\frac{Re}{\Delta t}\nabla\cdot\widetilde{\boldsymbol{u}}^{n+1}, \tag{29}$$

due to the condition $\nabla \cdot \boldsymbol{u}^{n+1} = 0$.

Here we use the fact that the Navier-Stokes Eq. (4c) could be written as

$$Re(\frac{\partial \boldsymbol{u}}{\partial t} + (\boldsymbol{u}\cdot\nabla)\boldsymbol{u}) = \nabla\cdot(\eta(\nabla\boldsymbol{u} + (\nabla\boldsymbol{u})^T)) - \nabla p - \frac{1}{Ca}\phi\nabla\tilde{\mu}_\phi - \frac{\beta}{Ca}(\zeta_+ C_+\nabla\mu_c^+ + \zeta_- C_-\nabla\mu_c^-).$$

Actually, the time discretization technique for the double-well potential $F(\phi)$ is the stabilized semi-implicit method. We assume that $F(\phi)$ satisfies the following condition: there exists a constant L such that

$$\max_\phi |F''(\phi)| \le L. \tag{30}$$

It is known that $F(\phi)$ does not satisfy (30). However, its has been a common practice [39] to consider the Cahn-Hilliard equation with a truncated double well potential $\tilde{F}(\phi)$. It is then obvious that there exists a constant L such that (30) is satisfied with $F(\phi)$ replaced by $\tilde{F}(\phi)$.

Theorem 4.1. *Assuming that the condition (30) is satisfied and $S \ge L/2$. Then the scheme (25)–(28) is energy stable and satisfies the following discrete energy law*

$$\begin{aligned}&\mathcal{E}^{n+1} - \mathcal{E}^n\\ &\le -\Delta t\eta||\nabla\widetilde{\boldsymbol{u}}^{n+1}||^2 - \frac{\Delta t\mathcal{M}}{Ca}||\nabla\tilde{\mu}_\phi^{n+1}||^2 - \frac{\Delta t}{Ca}\frac{K}{Ca}\int_\Omega |\tilde{\mu}_\phi^{n+1}|^2|\nabla\phi^n|d\boldsymbol{x} - \frac{\Delta t\beta}{CaPe}\sum_\pm\int_\Omega \zeta_\pm^n D_\pm^n C_\pm^{n+1}|\nabla\mu_{c_\pm}^{n+1}|^2\, d\boldsymbol{x}.\end{aligned}$$

where $||\cdot||$ denotes the discrete L^2 norm in domain Ω and

$$\mathcal{E}^n = \frac{Re}{2}||\boldsymbol{u}^n||^2 + \frac{1}{Ca}\left(\frac{\epsilon}{2}||\nabla\phi^n||^2 + \frac{\Delta t^2}{2Re}||\nabla p^n||^2 + \frac{1}{\epsilon}(F(\phi^n),1)\right) + \frac{\beta}{Ca}\sum_\pm\left(\zeta_\pm^n C_\pm^n(\ln C_\pm^n - 1), 1\right).$$

Proof. From (26), we have

$$Re\frac{\widetilde{\boldsymbol{u}}^{n+1} - \boldsymbol{u}^n}{\Delta t} + \frac{1}{Ca}\phi^n\nabla\tilde{\mu}_\phi^{n+1} + \frac{\beta}{Ca}\sum_\pm \zeta_\pm^n C_\pm^n\nabla\mu_{c_\pm}^{n+1} = Re\frac{\widetilde{\boldsymbol{u}}^{n+1} - \boldsymbol{u}_*^n}{\Delta t}.$$

Taking the inner product of (27) with $\Delta t\widetilde{\boldsymbol{u}}^{n+1}$, using the above relation, we derive

$$\frac{Re}{2}||\widetilde{\boldsymbol{u}}^{n+1}||^2 - \frac{Re}{2}||\boldsymbol{u}_*^n||^2 + \frac{Re}{2}||\widetilde{\boldsymbol{u}}^{n+1} - \boldsymbol{u}_*^n||^2 + \eta\Delta t||\nabla\widetilde{\boldsymbol{u}}^{n+1}||^2 + \Delta t(\nabla p^n, \widetilde{\boldsymbol{u}}^{n+1}) = 0. \tag{31}$$

To deal with the last term in the above, we first take the inner product of (28) with $\Delta t\nabla p^n$ to obtain

$$\frac{\Delta t^2}{2Re}(||\nabla p^{n+1}||^2 - ||\nabla p^n||^2 - ||\nabla p^{n+1} - \nabla p^n||^2) = \Delta t(\widetilde{\boldsymbol{u}}^{n+1}, \nabla p^n). \tag{32}$$

We also derive from (28) that

$$\frac{\Delta t^2}{2Re}||\nabla p^{n+1} - \nabla p^n||^2 = \frac{Re}{2}||\widetilde{\boldsymbol{u}}^{n+1} - \boldsymbol{u}^{n+1}||^2. \tag{33}$$

We then take the inner product of (28) with $\boldsymbol{u}^{n+1}$ to get

$$\frac{Re}{2}||\boldsymbol{u}^{n+1}||^2 + \frac{Re}{2}||\boldsymbol{u}^{n+1} - \widetilde{\boldsymbol{u}}^{n+1}||^2 = \frac{Re}{2}||\widetilde{\boldsymbol{u}}^{n+1}||^2. \tag{34}$$

Combining Eqs. (31)–(34), we find

$$\frac{Re}{2}||\boldsymbol{u}^{n+1}||^2 - \frac{Re}{2}||\boldsymbol{u}_*^n||^2 + \frac{Re}{2}||\widetilde{\boldsymbol{u}}^{n+1} - \boldsymbol{u}_*^n||^2 + \eta\Delta t||\nabla\widetilde{\boldsymbol{u}}^{n+1}||^2 + \frac{\Delta t^2}{2Re}(||\nabla p^{n+1}||^2 - ||\nabla p^n||^2) = 0. \tag{35}$$

Next, we use the relation (26) to deal with $||\boldsymbol{u}_*^n||^2$ in (35). Taking the inner product of (26) with $Re\boldsymbol{u}_*^n$, we obtain

$$\frac{Re}{2}||\boldsymbol{u}_*^n||^2 - \frac{Re}{2}||\boldsymbol{u}^n||^2 + \frac{Re}{2}||\boldsymbol{u}_*^n - \boldsymbol{u}^n||^2 = -\frac{\Delta t}{Ca}(\phi^n\nabla\tilde{\mu}_\phi^{n+1}, \boldsymbol{u}_*^n) - \frac{\beta\Delta t}{Ca}\sum_\pm(\zeta_\pm^n C_\pm^n\nabla\mu_{c_\pm}^{n+1}, \boldsymbol{u}_*^n). \tag{36}$$

Adding (35) and (36), we have

$$\begin{aligned}&\frac{Re}{2}||\boldsymbol{u}^{n+1}||^2 - \frac{Re}{2}||\boldsymbol{u}^n||^2 + \frac{Re}{2}||\widetilde{\boldsymbol{u}}^{n+1} - \boldsymbol{u}_*^n||^2 + \frac{Re}{2}||\boldsymbol{u}_*^n - \boldsymbol{u}^n||^2 + \eta\Delta t||\nabla\widetilde{\boldsymbol{u}}^{n+1}||^2\\ &+ \frac{\Delta t^2}{2Re}(||\nabla p^{n+1}||^2 - ||\nabla p^n||^2)\\ &= -\frac{\Delta t}{Ca}(\phi^n\nabla\tilde{\mu}_\phi^{n+1}, \boldsymbol{u}_*^n) - \frac{\beta\Delta t}{Ca}\sum_\pm(\zeta_\pm^n C_\pm^n\nabla\mu_{c_\pm}^{n+1}, \boldsymbol{u}_*^n).\end{aligned} \tag{37}$$

It now remains to deal with the last two terms in the above.

Taking the inner product of the first equation of (25) with $\frac{\Delta t}{Ca}\tilde{\mu}_\phi^{n+1}$, we get

$$\frac{1}{Ca}(\phi^{n+1} - \phi^n, \tilde{\mu}_\phi^{n+1}) = -\frac{\mathcal{M}\Delta t}{Ca}||\nabla\tilde{\mu}_\phi^{n+1}||^2 - \frac{\Delta t}{Ca}(\nabla\cdot(\boldsymbol{u}_*^n\phi^n), \tilde{\mu}_\phi^{n+1}) - \frac{\Delta t}{Ca}\frac{K}{Ca}\int_\Omega |\tilde{\mu}_\phi^{n+1}|^2|\nabla\phi^n|d\boldsymbol{x}, \tag{38}$$

and taking the inner product of the second equation of (25) with $-\frac{1}{Ca}(\phi^{n+1}-\phi^n)$, we obtain

$$\begin{aligned}-\frac{1}{Ca}(\tilde{\mu}_\phi^{n+1},\phi^{n+1}-\phi^n) =& -\frac{\epsilon}{2Ca}(||\nabla\phi^{n+1}||^2-||\nabla\phi^n||^2+||\nabla\phi^{n+1}-\nabla\phi^n||^2)\\ &+\frac{\beta}{Ca}\sum_{\pm}((\zeta_\pm^{n+1}-\zeta_\pm^n)C_\pm^{n+1},1)\\ &-\frac{1}{Ca\epsilon}(S(\phi^{n+1}-\phi^n)+f(\phi^n),\phi^{n+1}-\phi^n).\end{aligned}\tag{39}$$

For the last term in (39), we use the Taylor expansion

$$F(\phi^{n+1})-F(\phi^n)=f(\phi^n)(\phi^{n+1}-\phi^n)+\frac{f'(\xi_n)}{2}(\phi^{n+1}-\phi^n)^2.$$

Taking the inner product of the third equation of (25) with $\frac{\beta\Delta t}{Ca}\mu_{c_\pm}^{n+1}$, we have

$$\frac{\beta}{Ca}(\zeta_\pm^{n+1}C_\pm^{n+1}-\zeta_\pm^nC_\pm^n,\mu_{c_\pm}^{n+1})=-\frac{\beta\Delta t}{PeCa}\int_\Omega\zeta_\pm^nD_\pm^nC_\pm^{n+1}|\nabla\mu_{c_\pm}^{n+1}|^2\,d\boldsymbol{x}-\frac{\beta\Delta t}{Ca}(\nabla\cdot(\boldsymbol{u}_*^n\zeta_\pm^nC_\pm^n),\mu_{c_\pm}^{n+1}).\tag{40}$$

Combining (37)–(40), we have

$$\begin{aligned}&\frac{Re}{2}||\boldsymbol{u}^{n+1}||^2-\frac{Re}{2}||\boldsymbol{u}^n||^2+\frac{Re}{2}||\tilde{\boldsymbol{u}}^{n+1}-\boldsymbol{u}_*^n||^2+\frac{Re}{2}||\boldsymbol{u}_*^n-\boldsymbol{u}^n||^2+\eta\Delta t||\nabla\tilde{\boldsymbol{u}}^{n+1}||^2+\frac{\Delta t^2}{2Re}(||\nabla p^{n+1}||^2-||\nabla p^n||^2)\\ &+\frac{\mathcal{M}\Delta t}{Ca}||\nabla\tilde{\mu}_\phi^{n+1}||^2+\frac{\Delta t}{Ca}\frac{K}{Ca}\int_\Omega|\tilde{\mu}_\phi^{n+1}|^2|\nabla\phi^n|d\boldsymbol{x}+\frac{\epsilon}{2Ca}(||\nabla\phi^{n+1}||^2-||\nabla\phi^n||^2+||\nabla\phi^{n+1}-\nabla\phi^n||^2)\\ &+\frac{\beta\Delta t}{PeCa}\sum_\pm\int_\Omega\zeta_\pm^nD_\pm^nC_\pm^{n+1}|\nabla\mu_{c_\pm}^{n+1}|^2\,d\boldsymbol{x}+\frac{1}{Ca\epsilon}(F(\phi^{n+1})-F(\phi^n),1)+\frac{1}{Ca\epsilon}((S-\frac{f'(\xi_n)}{2})(\phi^{n+1}-\phi^n),\phi^{n+1}-\phi^n)\\ &+\frac{\beta}{Ca}\sum_\pm(\zeta_\pm^{n+1}C_\pm^{n+1}-\zeta_\pm^nC_\pm^n,\mu_{c_\pm}^{n+1})-\frac{\beta}{Ca}\sum_\pm((\zeta_\pm^{n+1}-\zeta_\pm^n)C_\pm^{n+1},1)=0.\end{aligned}\tag{41}$$

For the last two terms in the above, we use the following relation

$$\begin{aligned}&(\zeta_\pm^{n+1}C_\pm^{n+1}-\zeta_\pm^nC_\pm^n)\ln C_\pm^{n+1}-(\zeta_\pm^{n+1}-\zeta_\pm^n)C_\pm^{n+1}\\ =&[(\zeta_\pm^{n+1}-\zeta_\pm^n)C_\pm^{n+1}+\zeta_\pm^n(C_\pm^{n+1}-C_\pm^n)]\ln C_\pm^{n+1}-(\zeta_\pm^{n+1}-\zeta_\pm^n)C_\pm^{n+1}\\ =&(\zeta_\pm^{n+1}-\zeta_\pm^n)C_\pm^{n+1}(\ln C_\pm^{n+1}-1)+\zeta_\pm^n(C_\pm^{n+1}-C_\pm^n)\ln C_\pm^{n+1}\\ =&(\zeta_\pm^{n+1}-\zeta_\pm^n)C_\pm^{n+1}(\ln C_\pm^{n+1}-1)+\zeta_\pm^n(C_\pm^{n+1}-C_\pm^n)(\ln C_\pm^{n+1}-1)+\zeta_\pm^n(C_\pm^{n+1}-C_\pm^n).\end{aligned}$$

Using the Taylor expansion, it is easy to get

$$\ln C_\pm^{n+1}-\ln C_\pm^n=\frac{1}{C_\pm^n}(C_\pm^{n+1}-C_\pm^n)-\frac{1}{2\xi^2}(C_\pm^{n+1}-C_\pm^n)^2.$$

Combining the above two equalities, we find

$$\begin{aligned}&(\zeta_\pm^{n+1}C_\pm^{n+1}-\zeta_\pm^nC_\pm^n)\ln C_\pm^{n+1}-(\zeta_\pm^{n+1}-\zeta_\pm^n)C_\pm^{n+1}\\ =&\zeta_\pm^{n+1}C_\pm^{n+1}(\ln C_\pm^{n+1}-1)-\zeta_\pm^nC_\pm^n(\ln C_\pm^n-1)+\frac{\zeta_\pm^nC_\pm^n}{2\xi^2}(C_\pm^{n+1}-C_\pm^n)^2.\end{aligned}\tag{42}$$

Therefore, combining (41) and (42), we have the energy stability result. □

4.2. The fully-discrete LDG scheme and its energy stability

In this subsection, the LDG scheme to solve the scheme (25)–(28) is proposed.

Let $\mathcal{T}_h=\{K\}$ be a shape-regular subdivision of Ω. $\mathcal{E}_h$ denotes the union of the boundary faces of elements $K\in\mathcal{T}_h$, and $\mathcal{E}_0=\mathcal{E}_h\setminus\partial\Omega$. Let $\mathcal{P}^k(K)$ be the space of polynomials of degree at most $k\geq 0$ on $K\in\mathcal{T}_h$. The DG finite element spaces are denoted by

$$\begin{aligned}V_h=&\left\{\varphi:\quad \varphi|_K\in\mathcal{P}^k(K),\quad \forall K\in\mathcal{T}_h\right\},\\ \boldsymbol{W}_h=&\left\{\Phi=(\phi_1,\cdots,\phi_d)^T:\quad \phi_l|_K\in\mathcal{P}^k(K),\ \ l=1\cdots d,\quad \forall K\in\mathcal{T}_h\right\},\\ \boldsymbol{\Pi}_h=&\left\{\boldsymbol{\Theta}=(\theta_1,\cdots,\theta_d)^T:\quad \theta_l|_K\in(\mathcal{P}^k(K))^d,\ \ l=1\cdots d,\quad \forall K\in\mathcal{T}_h\right\}.\end{aligned}$$

To develop the LDG scheme, we first rewrite (25)–(28) as a first-order system

$$\frac{\phi^{n+1}-\phi^n}{\Delta t}=\mathcal{M}\nabla\cdot\boldsymbol{w}^{n+1}-\nabla\cdot\boldsymbol{q}^{n+1}-\frac{K}{Ca}\tilde{\mu}_\phi^{n+1}|\boldsymbol{v}^n|,\tag{43a}$$

$$\boldsymbol{w}^{n+1}=\nabla\tilde{\mu}_\phi^{n+1},\tag{43b}$$

$$\boldsymbol{q}^{n+1}=\phi^n\boldsymbol{u}_*^n,\tag{43c}$$

$$\tilde{\mu}_{\phi}^{n+1} = -\epsilon\nabla\cdot\boldsymbol{v}^{n+1} + \frac{S}{\epsilon}(\phi^{n+1}-\phi^{n}) + \frac{1}{\epsilon}f(\phi^{n}) - \beta\sum_{\pm}\frac{\zeta_{\pm}^{n+1}-\zeta_{\pm}^{n}}{\phi^{n+1}-\phi^{n}}C_{\pm}^{n+1}, \tag{43d}$$

$$\boldsymbol{v}^{n+1} = \nabla\phi^{n+1}, \tag{43e}$$

$$\frac{\zeta_{\pm}^{n+1}C_{\pm}^{n+1}-\zeta_{\pm}^{n}C_{\pm}^{n}}{\Delta t} = \frac{1}{Pe}\nabla\cdot\boldsymbol{w}_{\pm}^{n+1} - \nabla\cdot\boldsymbol{q}_{\pm}^{n+1}, \tag{43f}$$

$$\boldsymbol{w}_{\pm}^{n+1} = \zeta_{\pm}^{n}D_{\pm}^{n}C_{\pm}^{n+1}\boldsymbol{s}_{\pm}^{n+1}, \tag{43g}$$

$$\boldsymbol{s}_{\pm}^{n+1} = \nabla\mu_{c_{\pm}}^{n+1}, \tag{43h}$$

$$\mu_{c_{\pm}}^{n+1} = \ln C_{\pm}^{n+1}, \tag{43i}$$

$$\boldsymbol{q}_{\pm}^{n+1} = \boldsymbol{u}_{*}^{n}\zeta_{\pm}^{n}C_{\pm}^{n}, \tag{43j}$$

$$Re\frac{\widetilde{\boldsymbol{u}}^{n+1}-\boldsymbol{u}^{n}}{\Delta t} = \eta\nabla\cdot\boldsymbol{Q}^{n+1} - Re(\boldsymbol{u}^{n}\cdot\nabla)\widetilde{\boldsymbol{u}}^{n+1} - \boldsymbol{r}^{n} - \frac{1}{Ca}\phi^{n}\boldsymbol{w}^{n+1} - \frac{\beta}{Ca}\sum_{\pm}\zeta_{\pm}^{n}C_{\pm}^{n}\boldsymbol{s}_{\pm}^{n+1}, \tag{43k}$$

$$\boldsymbol{Q}^{n+1} = \nabla\widetilde{\boldsymbol{u}}^{n+1}, \tag{43l}$$

$$\boldsymbol{r}^{n+1} = \nabla p^{n+1}, \tag{43m}$$

$$Re\frac{\boldsymbol{u}^{n+1}-\widetilde{\boldsymbol{u}}^{n+1}}{\Delta t} = -(\boldsymbol{r}^{n+1}-\boldsymbol{r}^{n}), \tag{43n}$$

$$\nabla\cdot\boldsymbol{u}^{n+1} = 0. \tag{43o}$$

Then the LDG scheme to solve (43) is: find ϕ^{n+1}, $\tilde{\mu}_{\phi}^{n+1}$, $C_{\pm}^{n+1}$, $\mu_{c_{\pm}}^{n+1}$, $p^{n+1}\in V_h$, $\boldsymbol{w}^{n+1}$, $\boldsymbol{q}^{n+1}$, $\boldsymbol{v}^{n+1}$, $\boldsymbol{w}_{\pm}^{n+1}$, $\boldsymbol{s}_{\pm}^{n+1}$, $\boldsymbol{q}_{\pm}^{n+1}$, $\widetilde{\boldsymbol{u}}^{n+1}$, $\boldsymbol{u}^{n+1}$, $\boldsymbol{r}^{n+1}\in \boldsymbol{W}_h$, $\boldsymbol{Q}^{n+1}\in\boldsymbol{\Pi}_h$, such that, for all test functions φ_1, φ_2, φ_3, $\psi_{\pm}$, $\chi_{\pm}\in V_h$, $\boldsymbol{\theta}_1$, $\boldsymbol{\theta}_2$, $\boldsymbol{\theta}_3$, $\boldsymbol{\theta}_4$, $\boldsymbol{\theta}_5$, $\boldsymbol{\theta}_6$, $\boldsymbol{\varrho}_{\pm}$, $\boldsymbol{\varpi}_{\pm}$, $\boldsymbol{\vartheta}_{\pm}\in\boldsymbol{W}_h$, and $\boldsymbol{\Theta}\in\boldsymbol{\Pi}_h$, we have

$$\begin{aligned}\int_K\frac{\phi^{n+1}-\phi^{n}}{\Delta t}\varphi_1 dK =& -\int_K(\mathcal{M}\boldsymbol{w}^{n+1}-\boldsymbol{q}^{n+1})\cdot\nabla\varphi_1 dK + \int_{\partial K}(\mathcal{M}\widehat{\boldsymbol{w}}^{n+1}\\ &-\widehat{\boldsymbol{q}}^{n+1})\cdot\boldsymbol{n}\varphi_1 ds - \int_K\frac{K}{Ca}\tilde{\mu}_{\phi}^{n+1}|\boldsymbol{v}^{n}|\varphi_1 dK,\end{aligned} \tag{44a}$$

$$\int_K\boldsymbol{w}^{n+1}\cdot\boldsymbol{\theta}_1 dK = -\int_K\tilde{\mu}_{\phi}^{n+1}\nabla\cdot\boldsymbol{\theta}_1 dK + \int_{\partial K}\widehat{\tilde{\mu}}_{\phi}^{n+1}\boldsymbol{\theta}_1\cdot\boldsymbol{n}ds, \tag{44b}$$

$$\int_K\boldsymbol{q}^{n+1}\cdot\boldsymbol{\theta}_2 dK = \int_K\phi^{n}\boldsymbol{u}_{*}^{n}\cdot\boldsymbol{\theta}_2 dK, \tag{44c}$$

$$\begin{aligned}\int_K\tilde{\mu}_{\phi}^{n+1}\varphi_2 dK =& \epsilon\int_K\boldsymbol{v}^{n+1}\cdot\nabla\varphi_2 dK - \epsilon\int_{\partial K}\widehat{\boldsymbol{v}}^{n+1}\cdot\boldsymbol{n}\varphi_2 ds + \frac{1}{\epsilon}\int_K f(\phi^{n})\varphi_2 dK\\ &+\int_K\left(\frac{S}{\epsilon}(\phi^{n+1}-\phi^{n}) - \beta\sum_{\pm}\frac{\zeta_{\pm}^{n+1}-\zeta_{\pm}^{n}}{\phi^{n+1}-\phi^{n}}C_{\pm}^{n+1}\right)\varphi_2 dK,\end{aligned} \tag{44d}$$

$$\int_K\boldsymbol{v}^{n+1}\cdot\boldsymbol{\theta}_3 dK = -\int_K\phi^{n+1}\nabla\cdot\boldsymbol{\theta}_3 dK + \int_{\partial K}\widehat{\phi}^{n+1}\boldsymbol{\theta}_3\cdot\boldsymbol{n}ds, \tag{44e}$$

$$\begin{aligned}\int_K\frac{\zeta_{\pm}^{n+1}C_{\pm}^{n+1}-\zeta_{\pm}^{n}C_{\pm}^{n}}{\Delta t}\psi_{\pm}dK =& -\int_K(\frac{1}{Pe}\boldsymbol{w}_{\pm}^{n+1}-\boldsymbol{q}_{\pm}^{n+1})\cdot\nabla\psi_{\pm}dK\\ &+\int_{\partial K}(\frac{1}{Pe}\widehat{\boldsymbol{w}}_{\pm}^{n+1}-\widehat{\boldsymbol{q}}_{\pm}^{n+1})\cdot\boldsymbol{n}\psi_{\pm}ds,\end{aligned} \tag{44f}$$

$$\int_K\boldsymbol{w}_{\pm}^{n+1}\cdot\boldsymbol{\varrho}_{\pm}dK = \int_K\zeta_{\pm}^{n}D_{\pm}^{n}C_{\pm}^{n+1}\boldsymbol{s}_{\pm}^{n+1}\cdot\boldsymbol{\varrho}_{\pm}dK, \tag{44g}$$

$$\int_K\boldsymbol{s}_{\pm}^{n+1}\cdot\boldsymbol{\varpi}_{\pm}dK = -\int_K\mu_{c_{\pm}}^{n+1}\nabla\cdot\boldsymbol{\varpi}_{\pm}dK + \int_{\partial K}\widehat{\mu}_{c_{\pm}}^{n+1}\boldsymbol{\varpi}_{\pm}\cdot\boldsymbol{n}ds, \tag{44h}$$

$$\int_K\mu_{c_{\pm}}^{n+1}\chi_{\pm}dK = \int_K\ln C_{\pm}^{n+1}\chi_{\pm}dK, \tag{44i}$$

$$\int_K\boldsymbol{q}_{\pm}^{n+1}\cdot\boldsymbol{\vartheta}_{\pm}dK = \int_K\boldsymbol{u}_{*}^{n}\zeta_{\pm}^{n}C_{\pm}^{n}\cdot\boldsymbol{\vartheta}_{\pm}dK, \tag{44j}$$

$$\begin{aligned}Re\int_K\frac{\widetilde{\boldsymbol{u}}^{n+1}-\boldsymbol{u}^{n}}{\Delta t}\cdot\boldsymbol{\theta}_4 dK =& -\eta\int_K\boldsymbol{Q}^{n+1}\cdot\nabla\boldsymbol{\theta}_4 dK + \eta\int_{\partial K}(\widehat{\boldsymbol{Q}}^{n+1}\cdot\boldsymbol{n})\cdot\boldsymbol{\theta}_4 ds\\ &-\int_K(Re(\boldsymbol{u}^{n}\cdot\nabla)\widetilde{\boldsymbol{u}}^{n+1} + \boldsymbol{r}^{n} + \frac{1}{Ca}\phi^{n}\boldsymbol{w}^{n+1}\\ &+\frac{\beta}{Ca}\sum_{\pm}\zeta_{\pm}^{n}C_{\pm}^{n}\boldsymbol{s}_{\pm}^{n+1})\cdot\boldsymbol{\theta}_4 dK,\end{aligned} \tag{44k}$$

$$\int_K\boldsymbol{Q}^{n+1}\cdot\boldsymbol{\Theta}dK = -\int_K\widetilde{\boldsymbol{u}}^{n+1}\nabla\cdot\boldsymbol{\Theta}dK + \int_{\partial K}\widehat{\widetilde{\boldsymbol{u}}}^{n+1}\boldsymbol{\Theta}\cdot\boldsymbol{n}ds, \tag{44l}$$

$$\int_K \boldsymbol{r}^{n+1}\cdot\boldsymbol{\theta}_5 dK = -\int_K p^{n+1}\nabla\cdot\boldsymbol{\theta}_5 dK + \int_{\partial K}\widehat{p}^{n+1}\boldsymbol{\theta}_5\cdot\boldsymbol{n}ds, \tag{44m}$$

$$Re\int_K \frac{\boldsymbol{u}^{n+1}-\widetilde{\boldsymbol{u}}^{n+1}}{\Delta t}\cdot\boldsymbol{\theta}_6 dK = -\int_K(\boldsymbol{r}^{n+1}-\boldsymbol{r}^n)\cdot\boldsymbol{\theta}_6 dK, \tag{44n}$$

$$0 = -\int_K \boldsymbol{u}^{n+1}\cdot\nabla\varphi_3 dK + \int_{\partial K}\widehat{\boldsymbol{u}}_p^{n+1}\cdot\boldsymbol{n}\varphi_3 ds, \tag{44o}$$

with

$$\boldsymbol{u}_*^n = \boldsymbol{u}^n - \frac{\Delta t}{CaRe}\phi^n\boldsymbol{w}^{n+1} - \frac{\beta\Delta t}{CaRe}\sum_{\pm}\zeta_{\pm}^n C_{\pm}^n \boldsymbol{s}_{\pm}^{n+1}. \tag{45}$$

Here, the "hat" terms appearing in the cell-boundary contributions after integration by parts are the so-called numerical fluxes. These edge-based quantities are not uniquely defined and must be designed according to the structure of the underlying PDE system. In the present LDG formulation, the choice of numerical fluxes is guided mainly by consistency with the continuous model, preservation of the discrete energy stability, and local solvability of the intermediate variables.

Let e be an interior face shared by the "left" and "right" elements K_L and K_R and define the normal vectors $\boldsymbol{n}_L$ and $\boldsymbol{n}_R$ on e pointing exterior to K_L and K_R, respectively. For our purpose, "left" and "right" can be uniquely defined for each face according to any fixed rule. For example, we choose $\boldsymbol{n}_0$ as a constant vector. The left element K_L to the face requires that $\boldsymbol{n}_L\cdot\boldsymbol{n}_0 < 0$, and the right one K_R requires $\boldsymbol{n}_R\cdot\boldsymbol{n}_0 \geq 0$. If ψ is a function on K_L and K_R, but possibly discontinuous across e , let ψ_L denote $(\psi|_{K_L})|_e$ and ψ_R denote $(\psi|_{K_R})|_e$, the left and right trace, respectively.

In the following proof of the energy stability, we can see the alternating numerical fluxes can guarantee the energy stability, such as

$$\begin{aligned}
&\widehat{\boldsymbol{w}}^{n+1} = \boldsymbol{w}_L^{n+1}, \quad \widehat{\boldsymbol{q}}^{n+1} = \boldsymbol{q}_L^{n+1}, \quad \widehat{\tilde{\mu}}_{\phi}^{n+1} = \tilde{\mu}_{\phi,R}^{n+1}, \quad \widehat{\boldsymbol{v}}^{n+1} = \boldsymbol{v}_L^{n+1},\\
&\widehat{\phi}^{n+1} = \phi_R^{n+1}, \quad \widehat{\boldsymbol{q}}_{\pm}^{n+1} = \boldsymbol{q}_{\pm,L}^{n+1}, \quad \widehat{\boldsymbol{w}}_{\pm}^{n+1} = \boldsymbol{w}_{\pm,L}^{n+1}, \quad \widehat{\mu}_{c_{\pm}}^{n+1} = \mu_{c_{\pm},R}^{n+1},\\
&\widehat{\boldsymbol{Q}}^{n+1} = \boldsymbol{Q}_R^{n+1}, \quad \widehat{\widetilde{\boldsymbol{u}}}^{n+1} = \widetilde{\boldsymbol{u}}_L^{n+1}, \quad \widehat{p}^{n+1} = p_R^{n+1}, \quad \widehat{\boldsymbol{u}}_p^{n+1} = \boldsymbol{u}_L^{n+1}.
\end{aligned} \tag{46}$$

Under the boundary condition (2), the boundary numerical fluxes are

$$\widehat{\boldsymbol{w}}^{n+1}\cdot\boldsymbol{n} = 0,\ \widehat{\boldsymbol{q}}^{n+1} = \boldsymbol{0},\ \widehat{\boldsymbol{v}}^{n+1}\cdot\boldsymbol{n} = 0,\ \widehat{\boldsymbol{w}}_{\pm}^{n+1}\cdot\boldsymbol{n} = 0,\ \widehat{\boldsymbol{q}}_{\pm}^{n+1} = \boldsymbol{0},\ \widehat{\boldsymbol{u}}_p^{n+1} = \boldsymbol{0}, \tag{47}$$

and the rest boundary fluxes come from the interior of the domain.

For the convenience of presentation, we introduce some LDG operators. Denote

$$H_K^+(r,\boldsymbol{v}) = \int_K r\nabla\cdot\boldsymbol{v}dK - \int_{\partial K} r_R\boldsymbol{v}\cdot\boldsymbol{n}ds,\ H_K^-(\boldsymbol{v},r) = \int_K \boldsymbol{v}\cdot\nabla r dK - \int_{\partial K}\boldsymbol{v}_L\cdot\boldsymbol{n}r ds.$$

Summing up over K, we define

$$H^+(r,\boldsymbol{v}) = \sum_K H_K^+(r,\boldsymbol{v}), \qquad H^-(\boldsymbol{v},r) = \sum_K H_K^-(\boldsymbol{v},r).$$

With the special choice of the flux (46) and the boundary conditions (2), we have the property

$$H^+(r,\boldsymbol{v}) = -H^-(\boldsymbol{v},r). \tag{48}$$

Theorem 4.2. *Assume that condition (30) is satisfied and $S \geq L/2$. Then the solution to the fully-discrete LDG scheme (44) with the numerical fluxes (46) and the boundary conditions (47) satisfies the following discrete energy dissipation*

$$\mathcal{E}_h^{n+1} - \mathcal{E}_h^n \leq -\Delta t\int_\Omega\left(\eta|\boldsymbol{Q}^{n+1}|^2 + \frac{\mathcal{M}}{Ca}|\boldsymbol{w}^{n+1}|^2 + \frac{1}{Ca}\frac{K}{Ca}|\boldsymbol{v}^n||\tilde{\mu}_{\phi}^{n+1}|^2 + \sum_{\pm}\frac{\beta}{CaPe}\zeta_{\pm}^n D_{\pm}^n C_{\pm}^{n+1}|\boldsymbol{s}_{\pm}^{n+1}|^2\right)d\boldsymbol{x},$$

where

$$\mathcal{E}_h^n = \frac{Re}{2}\int_\Omega|\boldsymbol{u}^n|^2 d\boldsymbol{x} + \frac{1}{Ca}\int_\Omega\left(\frac{\epsilon}{2}|\boldsymbol{v}^n|^2 + \frac{1}{\epsilon}F(\phi^n)\right)d\boldsymbol{x} + \frac{\Delta t^2}{2Re}\int_\Omega|\boldsymbol{r}^n|^2 d\boldsymbol{x} + \frac{\beta}{Ca}\sum_{\pm}\int_\Omega\zeta_{\pm}^n C_{\pm}^n(\ln C_{\pm}^n - 1)d\boldsymbol{x}.$$

Proof. Taking the inner product of (45) with $\boldsymbol{u}_*^n$, we obtain

$$\frac{Re}{\Delta t}\int_K \boldsymbol{u}_*^n\cdot(\boldsymbol{u}_*^n - \boldsymbol{u}^n)dK = -\int_K\left(\frac{1}{Ca}\phi^n\boldsymbol{w}^{n+1} + \frac{\beta}{Ca}\sum_{\pm}\zeta_{\pm}^n C_{\pm}^n\boldsymbol{s}_{\pm}^{n+1}\right)\cdot\boldsymbol{u}_*^n dK. \tag{49}$$

From (45), we have

$$Re\frac{\widetilde{\boldsymbol{u}}^{n+1}-\boldsymbol{u}^n}{\Delta t} + \frac{1}{Ca}\phi^n\boldsymbol{w}^{n+1} + \frac{\beta}{Ca}\sum_{\pm}\zeta_{\pm}^n C_{\pm}^n\boldsymbol{s}_{\pm}^{n+1} = Re\frac{\widetilde{\boldsymbol{u}}^{n+1}-\boldsymbol{u}_*^n}{\Delta t}. \tag{50}$$

For (44k) of the LDG scheme, taking the test function $\boldsymbol{\theta}_4 = \widetilde{\boldsymbol{u}}^{n+1}$ and using the relation (50), we derive

$$Re\int_K\frac{\widetilde{\boldsymbol{u}}^{n+1}-\boldsymbol{u}_*^n}{\Delta t}\cdot\widetilde{\boldsymbol{u}}^{n+1}dK = -\eta\int_K\boldsymbol{Q}^{n+1}\cdot\nabla\widetilde{\boldsymbol{u}}^{n+1}dK + \eta\int_{\partial K}(\widehat{\boldsymbol{Q}}^{n+1}\cdot\boldsymbol{n})\cdot\widetilde{\boldsymbol{u}}^{n+1}ds$$

$$-\int_K (Re(\boldsymbol{u}^n\cdot\nabla)\widetilde{\boldsymbol{u}}^{n+1}+\boldsymbol{r}^n)\cdot\widetilde{\boldsymbol{u}}^{n+1}dK. \tag{51}$$

For the convenience of presentation, for any w we denote $\mathcal{D}w = w^{n+1}-w^n$. For (44e) and (44m), subtracting the equation at time level t^n from the equation at time level t^{n+1}, and choosing test functions $\boldsymbol{\theta}_3 = \frac{\epsilon}{Ca\Delta t}\boldsymbol{v}^{n+1}$, $\boldsymbol{\theta}_5 = \boldsymbol{u}^{n+1}$, we get

$$\frac{\epsilon}{Ca\Delta t}\int_K \mathcal{D}\boldsymbol{v}\cdot\boldsymbol{v}^{n+1}dK = -\frac{\epsilon}{Ca\Delta t}H_K^+(\mathcal{D}\phi,\boldsymbol{v}^{n+1}), \tag{52}$$

$$\int_K \mathcal{D}\boldsymbol{r}\cdot\boldsymbol{u}^{n+1}dK = -H_K^+(\mathcal{D}p,\boldsymbol{u}^{n+1}). \tag{53}$$

For (44a), (44b), (44c), (44d), (44f), (44g), (44h), (44i), (44j), (44l), (44n) and (44o) in the fully-discrete scheme, taking the test functions as

$$\varphi_1 = \frac{1}{Ca}\tilde{\mu}_\phi^{n+1},\quad \boldsymbol{\theta}_1 = \frac{1}{Ca}(\mathcal{M}\boldsymbol{w}^{n+1}-\boldsymbol{q}^{n+1}),\quad \boldsymbol{\theta}_2 = \frac{1}{Ca}\boldsymbol{w}^{n+1},\quad \varphi_2 = -\frac{1}{Ca\Delta t}\mathcal{D}\phi,$$
$$\psi_\pm = \frac{\beta}{Ca}\mu_{c_\pm}^{n+1},\quad \boldsymbol{\varrho}_\pm = -\frac{\beta}{CaPe}\boldsymbol{s}_\pm^{n+1},\quad \boldsymbol{\varpi}_\pm = \frac{\beta}{Ca}(\frac{1}{Pe}\boldsymbol{w}_\pm^{n+1}-\boldsymbol{q}_\pm^{n+1}),\quad \boldsymbol{\theta}_6 = \boldsymbol{u}^{n+1},$$
$$\chi_\pm = -\frac{\beta}{Ca\Delta t}(\zeta_\pm^{n+1}C_\pm^{n+1}-\zeta_\pm^n C_\pm^n),\quad \vartheta_\pm = \frac{\beta}{Ca}\boldsymbol{s}_\pm^{n+1},\quad \boldsymbol{\Theta} = \eta\boldsymbol{Q}^{n+1},\quad \varphi_3 = \mathcal{D}p.$$

We have

$$\frac{1}{Ca\Delta t}\int_K \mathcal{D}\phi\tilde{\mu}_\phi^{n+1}dK = -\frac{1}{Ca}H_K^-(\mathcal{M}\boldsymbol{w}^{n+1}-\boldsymbol{q}^{n+1},\tilde{\mu}_\phi^{n+1}) - \frac{1}{Ca}\frac{K}{Ca}\int_K|\boldsymbol{v}^n||\tilde{\mu}_\phi^{n+1}|^2dK, \tag{54}$$

$$\frac{1}{Ca}\int_K \boldsymbol{w}^{n+1}\cdot(\mathcal{M}\boldsymbol{w}^{n+1}-\boldsymbol{q}^{n+1})dK = -\frac{1}{Ca}H_K^+(\tilde{\mu}_\phi^{n+1},\mathcal{M}\boldsymbol{w}^{n+1}-\boldsymbol{q}^{n+1}), \tag{55}$$

$$\frac{1}{Ca}\int_K \boldsymbol{q}^{n+1}\cdot\boldsymbol{w}^{n+1}dK = \frac{1}{Ca}\int_K \phi^n\boldsymbol{u}_*^n\cdot\boldsymbol{w}^{n+1}dK, \tag{56}$$

$$-\frac{1}{Ca\Delta t}\int_K \tilde{\mu}_\phi^{n+1}\mathcal{D}\phi dK = -\frac{\epsilon}{Ca\Delta t}H_K^-(\boldsymbol{v}^{n+1},\mathcal{D}\phi)+\frac{\beta}{Ca\Delta t}\int_K\sum_\pm \mathcal{D}\zeta_\pm C_\pm^{n+1}dK - \frac{1}{Ca\Delta t}\int_K\Big(\frac{S}{\epsilon}(\mathcal{D}\phi)^2+\frac{1}{\epsilon}f(\phi^n)\mathcal{D}\phi\Big)dK, \tag{57}$$

$$\frac{\beta}{Ca\Delta t}\int_K(\zeta_\pm^{n+1}C_\pm^{n+1}-\zeta_\pm^nC_\pm^n)\mu_{c_\pm}^{n+1}dK = -\frac{\beta}{Ca}H_K^-(\frac{1}{Pe}\boldsymbol{w}_\pm^{n+1}-\boldsymbol{q}_\pm^{n+1},\mu_{c_\pm}^{n+1}), \tag{58}$$

$$-\frac{\beta}{CaPe}\int_K \boldsymbol{w}_\pm^{n+1}\cdot\boldsymbol{s}_\pm^{n+1}dK = -\frac{\beta}{CaPe}\int_K \zeta_\pm^n D_\pm^n C_\pm^{n+1}\boldsymbol{s}_\pm^{n+1}\cdot\boldsymbol{s}_\pm^{n+1}dK, \tag{59}$$

$$\frac{\beta}{Ca}\int_K \boldsymbol{s}_\pm^{n+1}\cdot(\frac{1}{Pe}\boldsymbol{w}_\pm^{n+1}-\boldsymbol{q}_\pm^{n+1})dK = -\frac{\beta}{Ca}H_K^+(\mu_{c_\pm}^{n+1},\frac{1}{Pe}\boldsymbol{w}_\pm^{n+1}-\boldsymbol{q}_\pm^{n+1}), \tag{60}$$

$$-\frac{\beta}{Ca\Delta t}\int_K \mu_{c_\pm}^{n+1}(\zeta_\pm^{n+1}C_\pm^{n+1}-\zeta_\pm^nC_\pm^n)dK = -\frac{\beta}{Ca\Delta t}\int_K \ln C_\pm^{n+1}(\zeta_\pm^{n+1}C_\pm^{n+1}-\zeta_\pm^nC_\pm^n)dK, \tag{61}$$

$$\frac{\beta}{Ca}\int_K \boldsymbol{q}_\pm^{n+1}\cdot\boldsymbol{s}_\pm^{n+1}dK = \frac{\beta}{Ca}\int_K \boldsymbol{u}_*^n\zeta_\pm^nC_\pm^n\cdot\boldsymbol{s}_\pm^{n+1}dK, \tag{62}$$

$$\eta\int_K \boldsymbol{Q}^{n+1}\cdot\boldsymbol{Q}^{n+1}dK = -\eta\int_K\widetilde{\boldsymbol{u}}^{n+1}\nabla\cdot\boldsymbol{Q}^{n+1}dK+\eta\int_{\partial K}\widehat{\widetilde{\boldsymbol{u}}}^{n+1}\boldsymbol{Q}^{n+1}\cdot\boldsymbol{n}ds, \tag{63}$$

$$Re\int_K\frac{\boldsymbol{u}^{n+1}-\widetilde{\boldsymbol{u}}^{n+1}}{\Delta t}\cdot\boldsymbol{u}^{n+1}dK = -\int_K(\boldsymbol{r}^{n+1}-\boldsymbol{r}^n)\cdot\boldsymbol{u}^{n+1}dK, \tag{64}$$

$$0 = -H_K^-(\boldsymbol{u}^{n+1},\mathcal{D}p). \tag{65}$$

Now combining the Eqs. (49), (51)–(65), summing over all elements K and by the property (48), we have

$$\begin{aligned}
&\frac{\epsilon}{Ca\Delta t}\int_\Omega \boldsymbol{v}^{n+1}\cdot(\boldsymbol{v}^{n+1}-\boldsymbol{v}^n)d\boldsymbol{x}+\frac{Re}{\Delta t}\int_\Omega \boldsymbol{u}^{n+1}\cdot(\boldsymbol{u}^{n+1}-\widetilde{\boldsymbol{u}}^{n+1})d\boldsymbol{x}\\
&+\frac{Re}{\Delta t}\int_\Omega \boldsymbol{u}_*^n\cdot(\boldsymbol{u}_*^n-\boldsymbol{u}^n)d\boldsymbol{x}+\frac{Re}{\Delta t}\int_\Omega\widetilde{\boldsymbol{u}}^{n+1}\cdot(\widetilde{\boldsymbol{u}}^{n+1}-\boldsymbol{u}_*^n)d\boldsymbol{x}+\frac{1}{Ca}\int_\Omega\mathcal{M}\boldsymbol{w}^{n+1}\cdot\boldsymbol{w}^{n+1}d\boldsymbol{x}\\
&+\frac{K}{Ca}\int_\Omega|\boldsymbol{v}^n||\tilde{\mu}_\phi^{n+1}|^2d\boldsymbol{x}+\frac{\beta}{CaPe}\sum_\pm\int_\Omega\zeta_\pm^nD_\pm^nC_\pm^{n+1}\boldsymbol{s}_\pm^{n+1}\cdot\boldsymbol{s}_\pm^{n+1}d\boldsymbol{x}\\
&+\eta\int_\Omega\boldsymbol{Q}^{n+1}\cdot\boldsymbol{Q}^{n+1}d\boldsymbol{x}+\int_\Omega\boldsymbol{r}^n\cdot\widetilde{\boldsymbol{u}}^{n+1}d\boldsymbol{x}+\frac{1}{Ca\Delta t}\int_\Omega\Big(\frac{S}{\epsilon}\mathcal{D}\phi+\frac{f(\phi^n)}{\epsilon}\Big)\mathcal{D}\phi d\boldsymbol{x}\\
&+\frac{\beta}{Ca\Delta t}\sum_\pm\int_\Omega\big(\ln C_\pm^{n+1}(\zeta_\pm^{n+1}C_\pm^{n+1}-\zeta_\pm^nC_\pm^n)-\mathcal{D}\zeta_\pm C_\pm^{n+1}\big)d\boldsymbol{x}=0.
\end{aligned} \tag{66}$$

For the last two terms in (66), we have

$$\begin{aligned}&\frac{1}{Ca}\int_\Omega\left(\frac{S}{\epsilon}\mathcal{D}\phi+\frac{f(\phi^n)}{\epsilon}\right)\mathcal{D}\phi d\boldsymbol{x}+\frac{\beta}{Ca}\sum_{\pm}\int_\Omega\left(\ln C_\pm^{n+1}(\zeta_\pm^{n+1}C_\pm^{n+1}-\zeta_\pm^nC_\pm^n)-\mathcal{D}\zeta_\pm C_\pm^{n+1}\right)d\boldsymbol{x}\\ =&\frac{1}{Ca\epsilon}\int_\Omega\left(F(\phi^{n+1})-F(\phi^n)\right)d\boldsymbol{x}+\frac{1}{Ca\epsilon}\int_\Omega\left(S-\frac{f'(\xi_n)}{2}\right)(\mathcal{D}\phi)^2d\boldsymbol{x}\\ &+\frac{\beta}{Ca}\sum_{\pm}\int_\Omega\left(\zeta_\pm^{n+1}C_\pm^{n+1}(\ln C_\pm^{n+1}-1)-\zeta_\pm^nC_\pm^n(\ln C_\pm^n-1)\right)d\boldsymbol{x}+\frac{\beta}{Ca}\sum_{\pm}\int_\Omega\frac{\zeta_\pm^nC_\pm^n}{2\xi^2}(\mathcal{D}C_\pm)^2d\boldsymbol{x}.\end{aligned}\tag{67}$$

To deal with the term $\int_\Omega \boldsymbol{r}^n\cdot\widetilde{\boldsymbol{u}}^{n+1}$, we take $\theta_6=\boldsymbol{r}^n$ and $\boldsymbol{r}^{n+1}$ in (44n), sum over all elements,

$$\frac{Re}{\Delta t}\int_\Omega\widetilde{\boldsymbol{u}}^{n+1}\cdot\boldsymbol{r}^nd\boldsymbol{x}=\frac{1}{2}\int_\Omega\left(|\boldsymbol{r}^{n+1}|^2-|\boldsymbol{r}^n|^2-|\boldsymbol{r}^{n+1}-\boldsymbol{r}^n|^2\right)d\boldsymbol{x},\tag{68}$$

$$\frac{Re}{\Delta t}\int_\Omega\widetilde{\boldsymbol{u}}^{n+1}\cdot\boldsymbol{r}^{n+1}d\boldsymbol{x}=\frac{1}{2}\int_\Omega\left(|\boldsymbol{r}^{n+1}|^2-|\boldsymbol{r}^n|^2+|\boldsymbol{r}^{n+1}-\boldsymbol{r}^n|^2\right)d\boldsymbol{x}.\tag{69}$$

where the term $\int_\Omega \boldsymbol{u}^{n+1}\cdot\boldsymbol{r}^nd\boldsymbol{x}$ is zero because of the divergence-free condition.

Using the above two equations and (44n) yield

$$\frac{Re^2}{\Delta t^2}\int_\Omega|\boldsymbol{u}^{n+1}-\widetilde{\boldsymbol{u}}^{n+1}|^2d\boldsymbol{x}=\int_\Omega|\boldsymbol{r}^{n+1}-\boldsymbol{r}^n|^2d\boldsymbol{x}.\tag{70}$$

Combining (68) and (70), we find

$$\int_\Omega\boldsymbol{r}^n\cdot\widetilde{\boldsymbol{u}}^{n+1}d\boldsymbol{x}=\frac{\Delta t}{2Re}\int_\Omega(|\boldsymbol{r}^{n+1}|^2-|\boldsymbol{r}^n|^2)d\boldsymbol{x}-\frac{Re}{2\Delta t}\int_\Omega|\boldsymbol{u}^{n+1}-\widetilde{\boldsymbol{u}}^{n+1}|^2d\boldsymbol{x}.\tag{71}$$

Combining (66), (67), and (71), we obtain

$$\begin{aligned}&\frac{\epsilon}{2Ca\Delta t}\int_\Omega\left(|\boldsymbol{v}^{n+1}|^2-|\boldsymbol{v}^n|^2\right)d\boldsymbol{x}+\frac{Re}{2\Delta t}\int_\Omega\left(|\boldsymbol{u}^{n+1}|^2-|\boldsymbol{u}^n|^2\right)d\boldsymbol{x}+\frac{\Delta t}{2Re}\int_\Omega\left(|\boldsymbol{r}^{n+1}|^2-|\boldsymbol{r}^n|^2\right)d\boldsymbol{x}\\ &+\frac{1}{Ca\epsilon\Delta t}\int_\Omega\left(F(\phi^{n+1})-F(\phi^n)\right)d\boldsymbol{x}+\frac{\beta}{Ca\Delta t}\sum_{\pm}\int_\Omega\left(\zeta_\pm^{n+1}C_\pm^{n+1}(\ln C_\pm^{n+1}-1)-\zeta_\pm^nC_\pm^n(\ln C_\pm^n-1)\right)d\boldsymbol{x}\\ \le&-\left(\frac{1}{Ca}\int_\Omega\mathcal{M}|\boldsymbol{Q}^{n+1}|^2d\boldsymbol{x}+\frac{1}{Ca}\frac{K}{Ca}\int_\Omega|\tilde{\mu}_\phi^{n+1}|^2|\boldsymbol{v}^n|d\boldsymbol{x}+\eta\int_\Omega|\boldsymbol{Q}^{n+1}|^2d\boldsymbol{x}+\frac{\beta}{CaPe}\sum_{\pm}\int_\Omega\zeta_\pm^nD_\pm^nC_\pm^{n+1}|\boldsymbol{s}_\pm^{n+1}|^2d\boldsymbol{x}\right),\end{aligned}$$

where we use the identity $a(a-b)=\frac{1}{2}a^2-\frac{1}{2}b^2+\frac{1}{2}(a-b)^2$ for $a=\boldsymbol{u}^{n+1},\boldsymbol{u}_*^n,\widetilde{\boldsymbol{u}}^{n+1},\boldsymbol{v}^{n+1}$, and $b=\widetilde{\boldsymbol{u}}^{n+1},\boldsymbol{u}^n,\boldsymbol{u}_*^n,\boldsymbol{v}^n$, respectively. Therefore, we have the energy stability result. □

4.3. The semi-implicit SDC method

The scheme proposed above is energy stable. However, it is limited to first-order temporal accuracy, while the LDG method is high-order accurate in space. To achieve high-order accuracy in time and space, we iteratively incorporate the semi-implicit spectral deferred correction (SDC) method [32,33], based on the energy-stabilized first-order scheme.

We now perform the SDC procedure over each time interval $[t^n,t^{n+1}]$. To do this, we divide the interval $[t^n,t^{n+1}]$ into P subintervals by selecting interpolation points $\{t^{n,m}\}_{m=0}^P$ such that

$$t^n=t^{n,0}<t^{n,1}<\cdots<t^{n,m}<\cdots<t^{n,P}=t^{n+1}.$$

Let $\Delta t^{n,m}=t^{n,m+1}-t^{n,m}$ and denote by $\phi_L^{n,m}$ the Lth-order approximation of $\phi(t^{n,m})$. To ensure high-order accuracy and avoid the instability associated with equispaced nodes, the time nodes $\{t^{n,m}\}_{m=0}^P$ can be chosen as the Chebyshev-Gauss-Lobatto points on $[t^n,t^{n+1}]$.

Starting from the known solution $(\phi^n,\boldsymbol{u}^n,C_\pm^n)$ at time t^n, we outline below the algorithm used to compute the updated solution $(\phi^{n+1},\boldsymbol{u}^{n+1},C_\pm^{n+1})$.

Compute the initial approximation:

Let $\phi_1^{n,0}=\phi^n$, $\boldsymbol{u}_1^{n,0}=\boldsymbol{u}^n$ and $C_{\pm,1}^{n,0}=C_\pm^n$.

Use the first-order scheme (25)–(28) to compute a first-order accurate approximate solution ϕ_1, $\boldsymbol{u}_1$ and $C_{\pm,1}$ at the nodes $\{t^{n,m}\}_{m=1}^P$, i.e.

For $m=0,\dots,P-1$

Step 1:

$$\begin{cases} \phi_1^{n,m+1} = \phi_1^{n,m} + \Delta t^{n,m}(\mathcal{M}\Delta\tilde{\mu}_{\phi,1}^{n,m+1} - \nabla\cdot(\phi_1^{n,m}\boldsymbol{u}_{*,1}^{n,m}) - \dfrac{K}{Ca}\tilde{\mu}_{\phi,1}^{n,m+1}|\nabla\phi_1^{n,m}|), \\ \tilde{\mu}_{\phi,1}^{n,m+1} = -\epsilon\Delta\phi_1^{n,m+1} + \dfrac{S}{\epsilon}(\phi_1^{n,m+1} - \phi_1^{n,m}) + \dfrac{1}{\epsilon}f(\phi_1^{n,m}) - \beta\displaystyle\sum_{\pm}\frac{\zeta_{\pm,1}^{n,m+1} - \zeta_{\pm,1}^{n,m}}{\phi_1^{n,m+1} - \phi_1^{n,m}}C_{\pm,1}^{n,m+1}, \\ \zeta_{\pm,1}^{n,m+1}C_{\pm,1}^{n,m+1} = \zeta_{\pm,1}^{n,m}C_{\pm,1}^{n,m} + \Delta t^{n,m}(\dfrac{1}{Pe}\nabla\cdot(\zeta_{\pm,1}^{n,m}D_{\pm,1}^{n,m}C_{\pm,1}^{n,m+1}\nabla\mu_{c_{\pm,1}}^{n,m+1}) - \nabla\cdot(\boldsymbol{u}_{*,1}^{n,m}\zeta_{\pm,1}^{n,m}C_{\pm,1}^{n,m})), \\ \mu_{c_{\pm,1}}^{n,m+1} = \ln C_{\pm,1}^{n,m+1}, \end{cases} \tag{72}$$

with

$$\boldsymbol{u}_{*,1}^{n,m} = \boldsymbol{u}_1^{n,m} - \frac{\Delta t^{n,m}}{CaRe}\phi_1^{n,m}\nabla\tilde{\mu}_{\phi,1}^{n,m+1} - \frac{\beta\Delta t^{n,m}}{CaRe}\sum_{\pm}\zeta_{\pm,1}^{n,m}C_{\pm,1}^{n,m}\nabla\mu_{c_{\pm,1}}^{n,m+1}; \tag{73}$$

Step 2:

$$\begin{aligned} \widetilde{\boldsymbol{u}}_1^{n,m+1} =& \boldsymbol{u}_1^{n,m} - \Delta t^{n,m}(\boldsymbol{u}_1^{n,m}\cdot\nabla)\widetilde{\boldsymbol{u}}_1^{n,m+1} \\ &+ \frac{\Delta t^{n,m}}{Re}(\eta\Delta\widetilde{\boldsymbol{u}}_1^{n,m+1} - \nabla p_1^{n,m} - \frac{1}{Ca}\phi_1^{n,m}\nabla\tilde{\mu}_{\phi,1}^{n,m+1} - \frac{\beta}{Ca}\sum_{\pm}\zeta_{\pm,1}^{n,m}C_{\pm,1}^{n,m}\nabla\mu_{c_{\pm,1}}^{n,m+1}); \end{aligned} \tag{74}$$

Step 3:

$$-\Delta(p_1^{n,m+1} - p_1^{n,m}) = -\frac{Re}{\Delta t^{n,m}}\nabla\cdot\widetilde{\boldsymbol{u}}_1^{n,m+1}, \tag{75}$$

$$\boldsymbol{u}_1^{n,m+1} = \widetilde{\boldsymbol{u}}_1^{n,m+1} - \frac{\Delta t^{n,m}}{Re}\nabla(p_1^{n,m+1} - p_1^{n,m}). \tag{76}$$

Compute successive corrections:

For $l = 1, \dots, L$,

Let $\phi_{l+1}^{n,0} = \phi^n$, $\boldsymbol{u}_{l+1}^{n,0} = \boldsymbol{u}^n$ and $C_{\pm,l+1}^{n,0} = C_\pm^n$.

For $m = 0, \dots, P-1$

Step 1:

$$\begin{cases} \phi_{l+1}^{n,m+1} =& \phi_{l+1}^{n,m} + \Delta t^{n,m}(\mathcal{M}\Delta\tilde{\mu}_{\phi,l+1}^{n,m+1} - \nabla\cdot(\phi_{l+1}^{n,m}\boldsymbol{u}_{*,l+1}^{n,m}) - \dfrac{K}{Ca}\tilde{\mu}_{\phi,l+1}^{n,m+1}|\nabla\phi_{l+1}^{n,m}| \\ & - \mathcal{M}\Delta\tilde{\mu}_{\phi,l}^{n,m+1} + \nabla\cdot(\phi_l^{n,m}\boldsymbol{u}_{*,l}^{n,m}) + \dfrac{K}{Ca}\tilde{\mu}_{\phi,l}^{n,m+1}|\nabla\phi_l^{n,m}|) + I_m^{m+1}(F_\phi), \\ \tilde{\mu}_{\phi,l+1}^{n,m+1} =& -\epsilon\Delta\phi_{l+1}^{n,m+1} + \dfrac{S}{\epsilon}(\phi_{l+1}^{n,m+1} - \phi_{l+1}^{n,m}) + \dfrac{1}{\epsilon}f(\phi_{l+1}^{n,m}) - \beta\displaystyle\sum_{\pm}\frac{\zeta_{\pm,l+1}^{n,m+1} - \zeta_{\pm,l+1}^{n,m}}{\phi_{l+1}^{n,m+1} - \phi_{l+1}^{n,m}}C_{\pm,l+1}^{n,m+1}, \\ \zeta_{\pm,l+1}^{n,m+1}C_{\pm,l+1}^{n,m+1} =& \zeta_{\pm,l+1}^{n,m}C_{\pm,l+1}^{n,m} + \Delta t^{n,m}(\dfrac{1}{Pe}\nabla\cdot(\zeta_{\pm,l+1}^{n,m}D_{\pm,l+1}^{n,m}C_{\pm,l+1}^{n,m+1}\nabla\mu_{c_{\pm,l+1}}^{n,m+1}) - \nabla\cdot(\boldsymbol{u}_{*,l+1}^{n,m}\zeta_{\pm,l+1}^{n,m}C_{\pm,l+1}^{n,m}) \\ & - \frac{1}{Pe}\nabla\cdot(\zeta_{\pm,l}^{n,m}D_{\pm,l}^{n,m}C_{\pm,l}^{n,m+1}\nabla\mu_{c_{\pm,l}}^{n,m+1}) + \nabla\cdot(\boldsymbol{u}_{*,l}^{n,m}\zeta_{\pm,l}^{n,m}C_{\pm,l}^{n,m})) + I_m^{m+1}(F_{c_\pm}), \\ \mu_{c_{\pm,l+1}}^{n,m+1} =& \ln C_{\pm,l+1}^{n,m+1}, \end{cases} \tag{77}$$

with

$$\boldsymbol{u}_{*,l+1}^{n,m} = \boldsymbol{u}_{l+1}^{n,m} - \frac{\Delta t^{n,m}}{CaRe}\phi_{l+1}^{n,m}\nabla\tilde{\mu}_{\phi,l+1}^{n,m+1} - \frac{\beta\Delta t^{n,m}}{CaRe}\sum_{\pm}\zeta_{\pm,l+1}^{n,m}C_{\pm,l+1}^{n,m}\nabla\mu_{c_{\pm,l+1}}^{n,m+1},$$

$$F_\phi = \mathcal{M}\Delta\tilde{\mu}_{\phi,l} - \nabla\cdot(\phi_l\boldsymbol{u}_l) - \frac{K}{Ca}\tilde{\mu}_{\phi,l}|\nabla\phi_l|,$$

$$F_{c_\pm} = \frac{1}{Pe}\nabla\cdot(\zeta_{\pm,l}D_{\pm,l}C_{\pm,l}\nabla\mu_{c_{\pm,l}}) - \nabla\cdot(\boldsymbol{u}_l\zeta_{\pm,l}C_{\pm,l});$$

Step 2:

$$\begin{aligned} \widetilde{\boldsymbol{u}}_{l+1}^{n,m+1} =& \boldsymbol{u}_{l+1}^{n,m} - \Delta t^{n,m}((\boldsymbol{u}_{l+1}^{n,m}\cdot\nabla)\widetilde{\boldsymbol{u}}_{l+1}^{n,m+1} - (\boldsymbol{u}_l^{n,m}\cdot\nabla)\widetilde{\boldsymbol{u}}_l^{n,m+1}) + \frac{\Delta t^{n,m}}{Re}(\eta\Delta\widetilde{\boldsymbol{u}}_{l+1}^{n,m+1} - \nabla p_{l+1}^{n,m} \\ & - \frac{1}{Ca}\phi_{l+1}^{n,m}\nabla\tilde{\mu}_{\phi,l+1}^{n,m+1} - \frac{\beta}{Ca}\sum_{\pm}\zeta_{\pm,l+1}^{n,m}C_{\pm,l+1}^{n,m}\nabla\mu_{c_{\pm,l+1}}^{n,m+1} - \eta\Delta\widetilde{\boldsymbol{u}}_l^{n,m+1} + \nabla p_l^{n,m} \\ & + \frac{1}{Ca}\phi_l^{n,m}\nabla\tilde{\mu}_{\phi,l}^{n,m+1} + \frac{\beta}{Ca}\sum_{\pm}\zeta_{\pm,l}^{n,m}C_{\pm,l}^{n,m}\nabla\mu_{c_{\pm,l}}^{n,m+1}) + I_m^{m+1}(F_{\boldsymbol{u}}), \end{aligned} \tag{78}$$

where

$$F_{\boldsymbol{u}} = -(\boldsymbol{u}_l\cdot\nabla)\widetilde{\boldsymbol{u}}_l + \frac{1}{Re}(\eta\Delta\widetilde{\boldsymbol{u}}_l - \nabla p_l - \frac{1}{Ca}\phi_l\nabla\tilde{\mu}_{\phi,l} - \frac{\beta}{Ca}\sum_{\pm}\zeta_{\pm,l}C_{\pm,l}\nabla\mu_{c_{\pm,l}});$$

Table 2
Temporal accuracy test. L^2 and L^∞ errors and orders of convergence at $T = 0.1$. The time step refinement path is taken to be $\Delta t = \Delta t_0/2^m$, $\Delta t_0 = 0.02$ and $m = 0, 1, 2, 3$.

	m	L^2 Err	Order	L^∞ Err	Order
ϕ	0	9.64E-03	–	3.10E-03	–
	1	5.02E-03	0.94	1.61E-03	0.95
	2	2.56E-03	0.97	8.27E-04	0.96
	3	1.29E-03	0.99	4.18E-04	0.98
$\boldsymbol{u}$	0	8.31E-03	–	3.17E-03	–
	1	4.09E-03	1.02	1.61E-03	0.98
	2	2.07E-03	0.98	8.18E-04	0.98
	3	1.04E-03	0.99	4.18E-04	0.97
C_+	0	4.55E-04	–	1.44E-04	–
	1	2.29E-04	0.99	7.34E-05	0.97
	2	1.15E-04	0.99	3.79E-05	0.95
	3	5.82E-05	0.98	1.93E-05	0.97

Step 3:

$$-(\Delta p_{l+1}^{n,m+1} - \Delta p_{l+1}^{n,m}) = -\frac{Re}{\Delta t^{n,m}}(\nabla\cdot\widetilde{\boldsymbol{u}}_{l+1}^{n,m+1} - \nabla\cdot\widetilde{\boldsymbol{u}}_{l}^{n,m+1}) + I_m^{m+1}(F), \tag{79}$$

$$\boldsymbol{u}_{l+1}^{n,m+1} = \widetilde{\boldsymbol{u}}_{l+1}^{n,m+1} + \frac{\Delta t^{n,m}}{Re}\nabla(p_{l+1}^{n,m+1} - p_{l+1}^{n,m}) - \frac{\Delta t^{n,m}}{Re}\nabla(p_{l}^{n,m+1} - p_{l}^{n,m}), \tag{80}$$

where

$$F = -\frac{Re}{(\Delta t^{n,m})^2}\nabla\cdot\widetilde{\boldsymbol{u}}_l.$$

Here, $I_m^{m+1}(F_\phi)$ is the integral of the P-th degree interpolating polynomial on the $P+1$ points $(t^{n,m}, F_\phi)_{m=0}^{P}$ over the subinterval $[t^{n,m}, t^{n,m+1}]$, which is the numerical quadrature approximation of

$$\int_{t^{n,m}}^{t^{n,m+1}} F_\phi dt.$$

Finally, we have $\phi^{n+1} = \phi_{L+1}^{n,P}$, $\boldsymbol{u}^{n+1} = \boldsymbol{u}_{L+1}^{n,P}$ and $C_\pm^{n+1} = C_{\pm,L+1}^{n,P}$.

Remark 4.1. (Local truncation error.) The local truncation error obtained with the above semi-implicit SDC scheme [33] is $\mathcal{O}(\tau^{\min[L+1,P+1]})$, where $\tau = \max_{n,m}\Delta t^{n,m}$.

5. Simulation results

In this section, we present numerical experiments that (i) verify the accuracy and stability of the proposed schemes and (ii) probe the model's mechanics. First, a space-time convergence study confirms the designed order of accuracy, and energy plots demonstrate unconditional decay for the first-order scheme together with the accuracy gains of the SDC upgrade. Second, a one-dimensional calibration in a no-flow setting shows that, as the interface thickness $\epsilon \to 0$, the phase-field solution converges to the sharp-interface limit. Finally, using the calibrated setup, we examine how membrane permeability K, solute concentration ratio, and imposed shear affect droplet evolution and equilibrium morphology, highlighting how osmotic-hydrostatic competition and semi-permeability regulate droplet volume.

Example 5.1 (Accuracy tests and energy stability test)**.** Consider the model (4) in the domain $\Omega = [0, 2\pi]\times[0, 2\pi]$. For the tests, we choose a suitable term such that the exact solution is taken as

$$\phi(x, y, t) = 0.3 + 0.2e^{-2t}\sin(x)\sin(y),$$
$$\boldsymbol{u}(x, y, t) = (-0.25e^{-2t}\sin^2(x)\sin(2y), 0.25e^{-2t}\sin(2x)\sin^2(y)),$$
$$C_+(x, y, t) = 0.2 + 0.1e^{-2t}\cos(x)\cos(y),\ C_-(x, y, t) = 0.2 + 0.1e^{-2t}\sin(x)\sin(y).$$

Choose the parameters $\mathcal{M} = K = \epsilon = \beta = Pe = Ca = Re = \eta = 1$.

To test the temporal accuracy of the scheme (44), we let $N = 64$ and $\mathcal{P}^2$ approximation to ensure that the spatial discretization error is small enough, and then the temporal discretization error is dominant. The time step refinement path is taken to be $\Delta t = \Delta t_0/2^m$, $\Delta t_0 = 0.02$ and $m = 0, 1, 2, 3$. The L^2 and L^∞ errors and orders of convergence are presented in Table 2, which shows first-order accurate in time.

Table 3
Spatial and temporal accuracy for second-order SDC with $\mathcal{P}^1$ and third-order SDC with $\mathcal{P}^2$ elements. L^2 and L^∞ errors and convergence orders at $T = 0.2$ with $\Delta t = 0.1\Delta x$.

Variable	N	$\mathcal{P}^1$				$\mathcal{P}^2$			
		L^2 Err	Order	L^∞ Err	Order	L^2 Err	Order	L^∞ Err	Order
ϕ	8	3.26E-02	–	2.42E-02	–	3.96E-03	–	3.72E-03	–
	16	8.74E-03	1.90	6.80E-03	1.83	4.94E-04	3.01	4.63E-04	3.01
	32	2.28E-03	1.94	1.78E-03	1.93	6.19E-05	3.00	5.66E-05	3.03
	64	5.88E-04	1.96	4.57E-04	1.96	7.90E-06	2.97	7.18E-06	2.98
$\boldsymbol{u}$	8	9.60E-02	–	7.67E-02	–	2.10E-02	–	1.95E-02	–
	16	2.35E-02	2.02	2.08E-02	1.88	2.65E-03	2.98	2.75E-03	2.83
	32	5.98E-03	1.98	5.45E-03	1.94	3.33E-04	3.00	3.39E-04	3.02
	64	1.50E-03	1.99	1.38E-03	1.98	4.23E-05	2.98	4.20E-05	3.01
C_+	8	1.58E-02	–	1.16E-02	–	2.01E-03	–	1.97E-03	–
	16	3.95E-03	2.00	3.00E-03	1.96	2.49E-04	3.01	2.32E-04	3.08
	32	9.77E-04	2.02	7.30E-04	2.04	3.17E-05	2.97	2.90E-05	3.00
	64	2.43E-04	2.01	1.78E-04	2.03	4.03E-06	2.98	3.66E-06	2.99

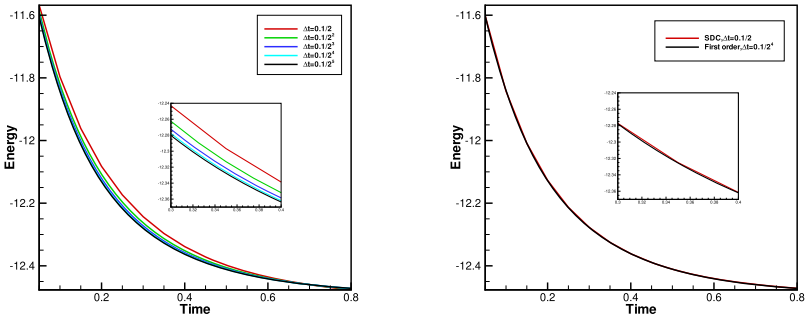

(a) First order scheme (b) Second order SDC scheme

Fig. 2. Energy evolution of the first-order scheme and the second order SDC scheme.

The L^2 and L^∞ errors, along with the observed convergence orders, are summarized in Table 3 for both second-order SDC with $\mathcal{P}^1$ elements and third-order SDC with $\mathcal{P}^2$ elements. As expected, the second-order SDC scheme exhibits consistent second-order convergence in both norms for all variables when using $\mathcal{P}^1$ elements. Similarly, the third-order SDC scheme coupled with $\mathcal{P}^2$ elements achieves third-order accuracy in both spatial and temporal directions. These results confirm the effectiveness of the proposed LDG–SDC framework in achieving high-order accuracy while maintaining numerical stability, even under relatively large time step sizes.

Fig. 2(a) presents the energy evolution of the scheme (44) for various time steps, ranging from $\Delta t = 0.1/2$ to $\Delta t = 0.1/2^5$, using a $\mathcal{P}^1$ approximation with a fixed mesh size $\Delta x = \Delta y = 2\pi/64$. The energy curves consistently exhibit monotonic decay across all time step sizes, in agreement with the theoretical guarantee of unconditional energy stability.

For larger time steps ($\Delta t = 0.1/2, 0.1/2^2, 0.1/2^3$), noticeable deviations from the reference energy curve (computed with $\Delta t = 0.1/2^5$) are observed, reflecting the reduced accuracy of the first-order temporal scheme. This highlights the necessity of smaller time steps to achieve high-fidelity solutions.

By contrast, our semi-implicit SDC scheme significantly improves temporal accuracy. As illustrated in Fig. 2(b), the energy curve of the second-order SDC scheme with $\Delta t = 0.1/2$ closely matches the reference energy curve computed with $\Delta t = 0.1/2^4$, demonstrating the effectiveness of the SDC method in achieving both stability and high-order accuracy.

Example 5.2 (1D calibration: diffuse–sharp correspondence in the no-flow setting)**.** We design a lightweight one-dimensional (1D) calibration to validate the diffuse-sharp correspondence of the phase-field profile in the *no-flow* setting ($\boldsymbol{u} \equiv 0$). The associated sharp-interface model on $\Omega = [0, 1]$ reads

$$\partial_t C_\pm = \frac{1}{Pe}\,\partial_x\big(D_\pm\,\partial_x C_\pm\big) \quad \text{in } \Omega^\pm(t),$$

with no-flux (Neumann) boundary conditions at $x = 0, 1$ and an impermeable interface on $\Gamma(t)$. The interface position $x_\Gamma(t)$ evolves by

$$\frac{dx_\Gamma}{dt} = -\frac{\beta}{Ca}\,\tilde{K}\,\big(C^+ - C^-\big)\Big|_{x=x_\Gamma(t)}.$$

We initialize

$$\Omega^+(0) = [0, 0.5], \quad \Omega^-(0) = [0.5, 1], \qquad C_+(x,0) = C_L = 0.2, \quad C_-(x,0) = C_R = 0.3.$$

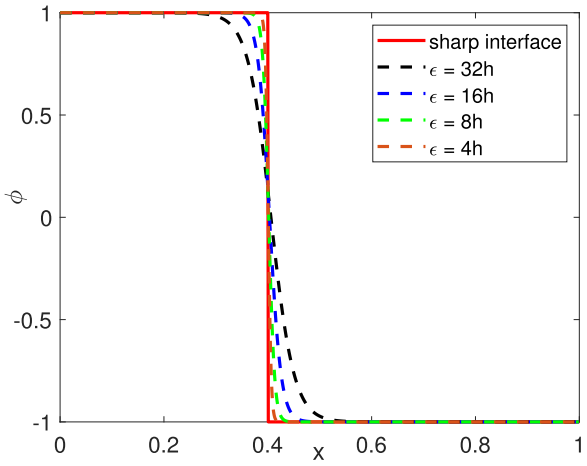

Fig. 3. Sharp-interface vs. phase-field in 1D. The red solid line marks the sharp-interface partition at $x_\Gamma^{\mathrm{eq}} = 0.4$; dashed curves are phase-field profiles ϕ^{eq} with $\epsilon = 32h, 16h, 8h, 4h$. As ϵ decreases, the diffuse interface converges to the sharp indicator. (For interpretation of the references to colour in this figure legend, the reader is referred to the web version of this article.)

Because the interface is impermeable to solute and the external boundaries are Neumann, the solute mass in each compartment is conserved while diffusion drives $C_\pm$ to piecewise constants. At equilibrium,

$$C_+^{\mathrm{eq}} = C_-^{\mathrm{eq}} = \frac{C_L + C_R}{2}, \qquad x_\Gamma^{\mathrm{eq}} = \frac{C_L}{C_L + C_R} = 0.4,$$

and the sharp indicator of the inner domain is

$$\mathbb{I}_{\Omega^+}(x) = \begin{cases} 1, & x < x_\Gamma^{\mathrm{eq}}, \\ -1, & x > x_\Gamma^{\mathrm{eq}}. \end{cases}$$

For the phase-field description, we solve

$$\partial_t \phi = \partial_x\big(\mathcal{M}\,\partial_x \tilde{\mu}_\phi\big) - \frac{K}{Ca}\,\tilde{\mu}_\phi\,\big|\partial_x \phi\big|, \tag{81a}$$

$$\partial_t(\zeta_\pm C_\pm) = \frac{1}{Pe}\,\partial_x\big(\zeta_\pm D_\pm\,\partial_x C_\pm\big), \tag{81b}$$

$$\tilde{\mu}_\phi = -\epsilon\,\partial_{xx}\phi + \frac{1}{\epsilon}F'(\phi) - \beta\big(\zeta_+'(\phi)\,C_+ + \zeta_-'(\phi)\,C_-\big), \tag{81c}$$

subject to no-flux conditions at $x = 0, 1$ and the initial data

$$\phi(x,0) = \tanh\Big(\frac{0.5 - x}{\sqrt{2}\,\epsilon}\Big), \qquad C_+(x,0) = C_L, \quad C_-(x,0) = C_R.$$

To quantify the diffuse-sharp agreement at equilibrium, we compare the sharp-interface domain index function $\mathbb{I}_\Omega$ with the phase-field solution ϕ^{eq}. We perform a resolution study with $\epsilon \in \{32h, 16h, 8h, 4h\}$, where $h = 1/1024$ is the mesh size in Fig. 3. This isolates the diffuse-to-sharp mapping (with fluid neglected) and numerically confirms that $\phi^{\mathrm{eq}} \to \mathbb{I}_{\Omega^+}$ as $\epsilon \to 0$, consistent with the sharp-interface limit.

Example 5.3 (Effects of permeability K)**.** In this example, we consider how the permeability affects the equilibrium shapes of droplets. Consider the model (4) in the domain $\Omega = [0, 6.4] \times [0, 6.4]$. The initial profiles of concentration and interface are given as follows (see Fig. 4)

$$\phi(x,y,0) = \tanh\left(\frac{1.0 - \sqrt{(x-3.2)^2 + (y-3.2)^2}}{\sqrt{2}\epsilon}\right),$$

$$\boldsymbol{u}(x,y,0) = \mathbf{0},$$

$$C_+(x,y,0) = c_0 + \exp\left(-\frac{(x-3.2)^2 + (y-3.2)^2}{0.15}\right),$$

$$C_-(x,y,0) = 0.02,$$

with parameters

$$\mathcal{M} = 0.03, \epsilon = 0.03, Re = 1, Pe = 1, \eta = 1, Ca = 1, \beta = 2,$$

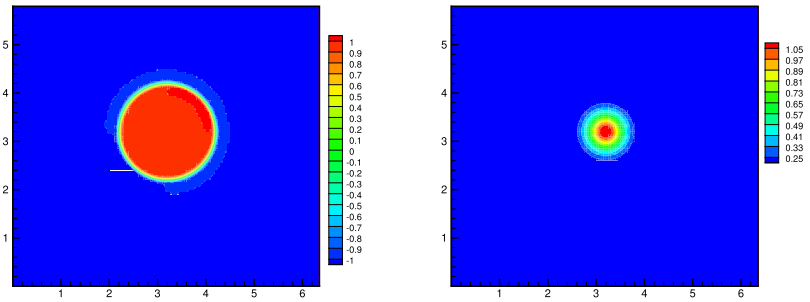

(a) Initial condition of ϕ (b) Initial condition of C_+

Fig. 4. Initial condition for Example 5.3 with $c_0 = 0.15$.

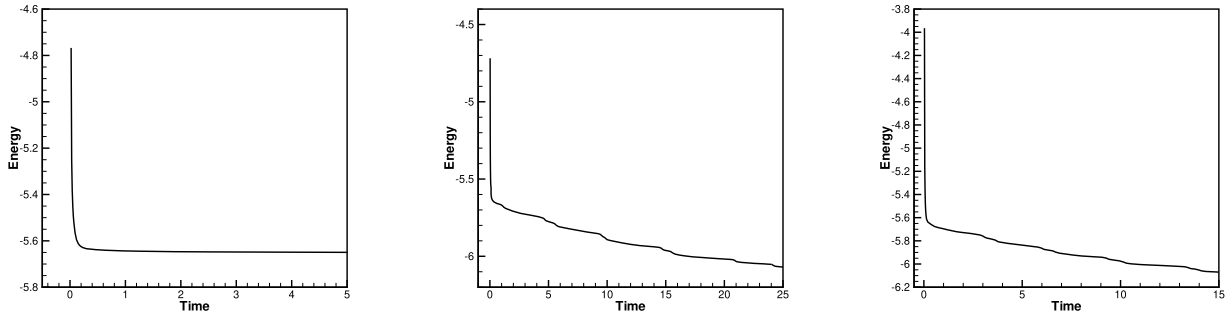

(a) $K = 0$ (b) $K = 0.1$ (c) $K = 0.3$

Fig. 5. Time evolution of the free energy functional with different permeability: $K = 0, 0.1$ and 0.3 with $c_0 = 0.15$.

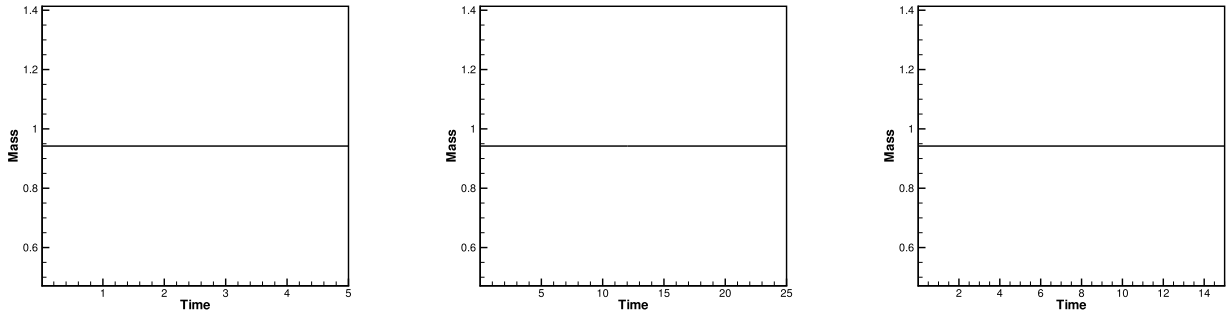

(a) $K = 0$ (b) $K = 0.1$ (c) $K = 0.3$

Fig. 6. Time evolution of the mass ($\int_\Omega \zeta_+ C_+ d\boldsymbol{x}$) with different permeability: $K = 0, 0.1$ and 0.3 with $c_0 = 0.15$.

where the substance is concentrated inside the droplet center (see Fig. 4 (b)). Two different initial concentration cases are considered: $c_0 = 0.15$ and $c_0 = 0.1$, each with three different permeabilities: $K = 0$, 0.1, and 0.3. Additionally, a reference case with no solute, where cross-interface flow is driven purely by hydrostatic pressure, is included for comparison to highlight the effects of osmotic pressure.

We employ the second-order SDC method with a piecewise $\mathcal{P}^1$ polynomial basis. The computational domain consists of a uniform mesh with 128×128 elements, and the time step is set to $\Delta t = 0.01$.

For the case $c_0 = 0.15$, the evolutions of energy and mass are presented in Figs. 5 and 6. As expected, the energy decreases over time, confirming the stability of the scheme, while the total mass remains conserved throughout the simulation.

Fig. 7 displays the evolution of droplet interfaces under different membrane permeabilities. The corresponding concentration profiles at equilibrium are shown in Fig. 8. When the permeability $K = 0$, water cannot cross the membrane, so the droplet retains its initial volume. In contrast, when $K \neq 0$, the initial hydrostatic pressure inside the droplet exceeds the osmotic pressure outside, driving water outward and causing the droplet to shrink. Since the solute remains confined within the droplet, the volume loss increases the

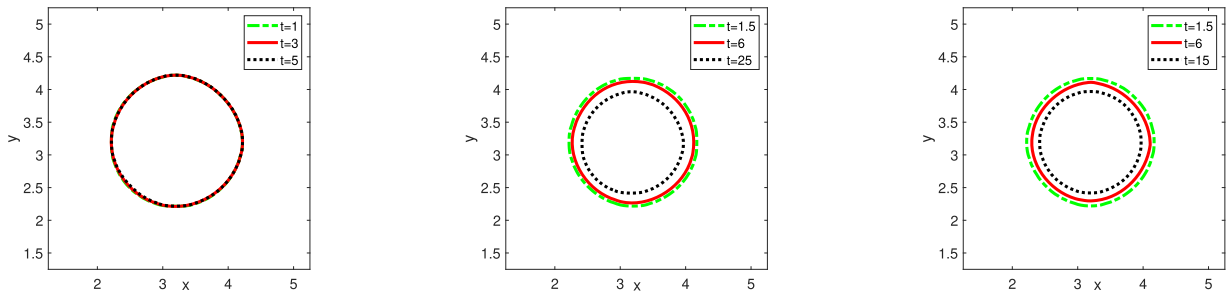

(a) $K = 0$ (b) $K = 0.1$ (c) $K = 0.3$

Fig. 7. Snapshots of interface $\phi = 0$ at different time slots with different permeability: $K = 0, 0.1$ and 0.3 with $c_0 = 0.15$.

internal solute concentration, thereby raising the osmotic pressure. This elevated osmotic pressure gradually draws water back into the droplet until equilibrium is reached, where the hydrostatic and osmotic pressures are balanced.

According to the energy dissipation law stated in Theorem 2.1, for a closed system, the equilibrium state is characterized by the conditions

$$\boldsymbol{u} = 0, \quad \tilde{\mu}_\phi = 0, \quad \mu_c^{\pm} = 0,$$

which implies that the droplet shape at equilibrium is independent of the membrane permeability K, and is determined solely by surface tension and the solute concentration difference across the interface. At equilibrium, the concentrations $C_\pm$ inside and outside the droplet become spatially uniform, with their values determined by the total initial solute mass and the geometry of the final droplet. These behaviors are clearly observed in Figs. 7 and 8. The role of permeability primarily affects the rate at which equilibrium is reached. Higher permeability leads to faster cross-interface water exchange, accelerating droplet shrinkage and energy dissipation. Consequently, systems with larger K values reach equilibrium more rapidly, as demonstrated in Figs. 5 and 7.

Example 5.4 (Effect of solute concentration)**.** To quantify how solute concentration influences the final droplet volume, we compare two scenarios: (i) *no solute* (osmotic effects neglected), in which case the system reduces to the CHNS model with a Allen-Cahn-type term $-\frac{K}{Ca}\tilde{\mu}_\phi |\nabla\phi|$ drives cross-interface flow purely by hydrostatic pressure; and (ii) *nonzero solute* with uniform initial concentrations $c_0 \in \{0.1, 0.3, 0.5\}$ inside the droplet. During the simulation, we repeat the setup of the previous example but *fix* the permeability and interface thickness to $K = 0.5$ and $\epsilon = 0.05$ (all other parameters and the initial geometry are unchanged).

As shown in Fig. 9, when osmotic effects are neglected, the droplet eventually vanishes-consistent with previous studies. In contrast, when osmotic pressure is included the droplet evolves toward a finite equilibrium configuration, and the final interface profile depends on the initial solute concentration c_0 (see Fig. 10).

For $c_0 = 0.1$ and 0.3, the droplet first shrinks as hydrostatic pressure dominates; the accompanying volume loss raises the interior concentration and hence the osmotic counter-pressure. Around $t \approx 20$, the osmotic and hydrostatic pressures balance, and a steady radius is reached. A larger c_0 arrests shrinkage earlier and yields a larger equilibrium droplet. For $c_0 = 0.5$, the initial osmotic pressure already exceeds the hydrostatic pressure, driving water influx and a swelling phase, which leads to the largest equilibrium volume among the cases considered.

We also compare our simulations with the sharp-interface model (23) and (24). At steady state, the normal solvent flux across the interface vanishes and the normal-stress jump balances the osmotic jump. For a circular interface of radius R^{eq} (curvature $\kappa = 1/R^{eq}$), this gives

$$\frac{\sigma}{R^{eq}} = \beta\left(C_+^{eq} - C_-^{eq}\right), \tag{82}$$

where the sign corresponds to the outward normal pointing from the inner to the outer phase. Mass conservation in each compartment yields

$$N_{\text{in}} := \int_\Omega C_+(x,0)\,\zeta_+(\phi(x,0))\,dx = \pi(R^{eq})^2\,C_+^{eq}, \;\; N_{\text{out}} := \int_\Omega C_-(x,0)\,\zeta_-(\phi(x,0))\,dx = \left(L^2 - \pi(R^{eq})^2\right)C_-^{eq}.$$

Eliminating $C_\pm^{eq}$ from above two equations gives a single nonlinear equation for R^{eq}:

$$\beta\left(\frac{N_{\text{in}}}{\pi(R^{eq})^2} - \frac{N_{\text{out}}}{L^2 - \pi(R^{eq})^2}\right) = \frac{\sigma}{R^{eq}}, \tag{83}$$

from which R^{eq} is determined uniquely in $0 < R^{eq} < L/\sqrt{\pi}$; the corresponding equilibrium concentrations follow as $C_+^{eq} = N_{\text{in}}/\left(\pi(R^{eq})^2\right)$ and $C_-^{eq} = N_{\text{out}}/\left(L^2 - \pi(R^{eq})^2\right)$. Fig. 9 shows that the phase-field predictions for the equilibrium radius and the inner/outer concentrations agree closely with the sharp-interface values obtained from (83), confirming that the diffuse-interface formulation is consistent with the sharp-interface limit.

These results also illustrate that the proposed permeation mechanism is bidirectional. For $c_0 = 0.1$ and 0.3, the droplet initially shrinks because the hydrostatic contribution dominates the osmotic one; as the droplet loses water, the interior solute concentration

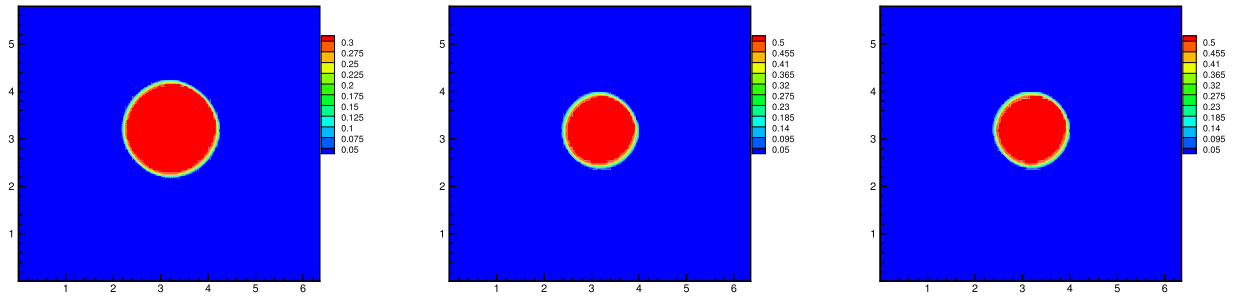

(a) $K = 0$ (b) $K = 0.1$ (c) $K = 0.3$

Fig. 8. Snapshots of $\zeta_+ C_+$ at equilibrium with different permeability: $K = 0, 0.1$ and 0.3 with $c_0 = 0.15$.

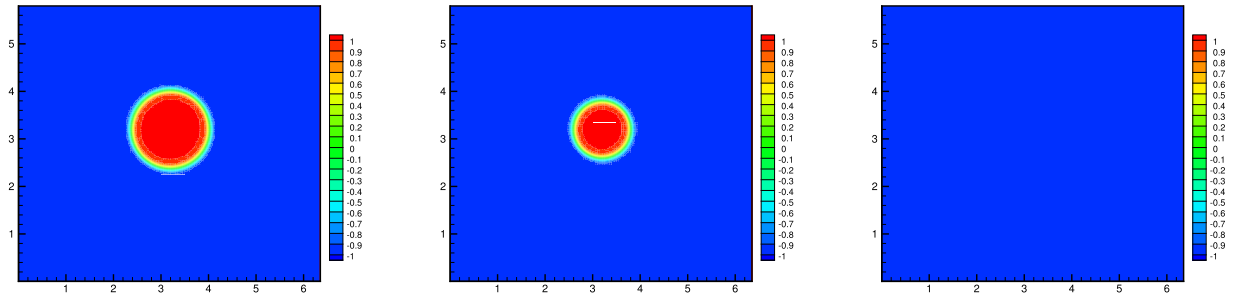

(a) $t = 1$ (b) $t = 2$ (c) $t = 4$

Fig. 9. The profiles of the interface when the osmotic pressure is neglected at time slots $t = 1, 2, 4$ with permeability $K = 0.5$.

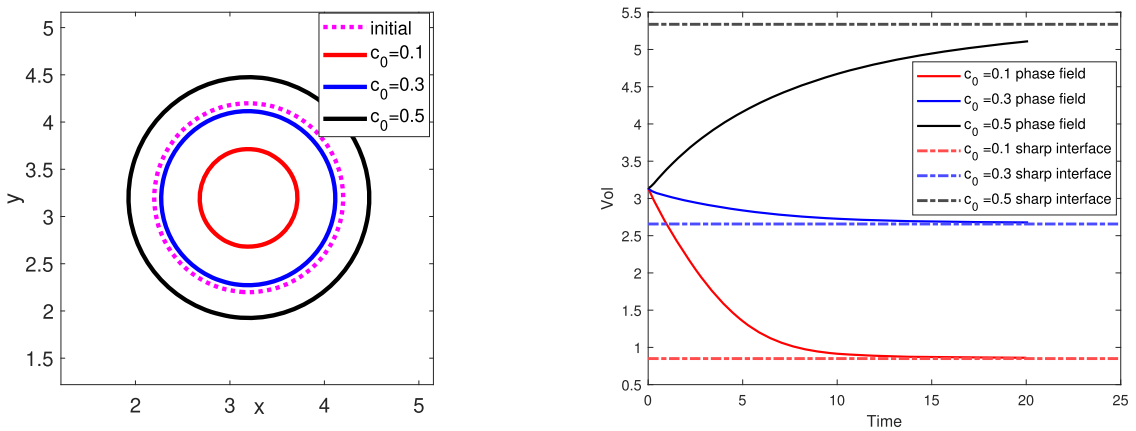

(a) Droplet profile at equilibrium (b) Volume over time

Fig. 10. Effect of solute concentration on droplet profile. (a) The droplet profile at equilibrium. (b) The evolution of droplet volumes with different initial solution concentrations. The red lines: $c_0 = 0.1$; the blue lines: $c_0 = 0.3$; the black lines: $c_0 = 0.5$; the dashed pink line: initial interface. The solid lines are the phase field model results, and the dashed lines are the sharp interface volume estimation at the equilibrium. (For interpretation of the references to colour in this figure legend, the reader is referred to the web version of this article.)

increases, which strengthens the opposing osmotic pressure until a balance is reached. In contrast, for $c_0 = 0.5$, the initial osmotic pressure is already sufficiently strong to overcome the hydrostatic resistance, so water enters the droplet and an initial swelling phase is observed before the system relaxes to equilibrium. Therefore, the model supports both inward and outward solvent transport across the semipermeable interface, and the direction of volume change is selected by the instantaneous osmotic-hydrostatic balance rather than by the sign of the permeability parameter itself.

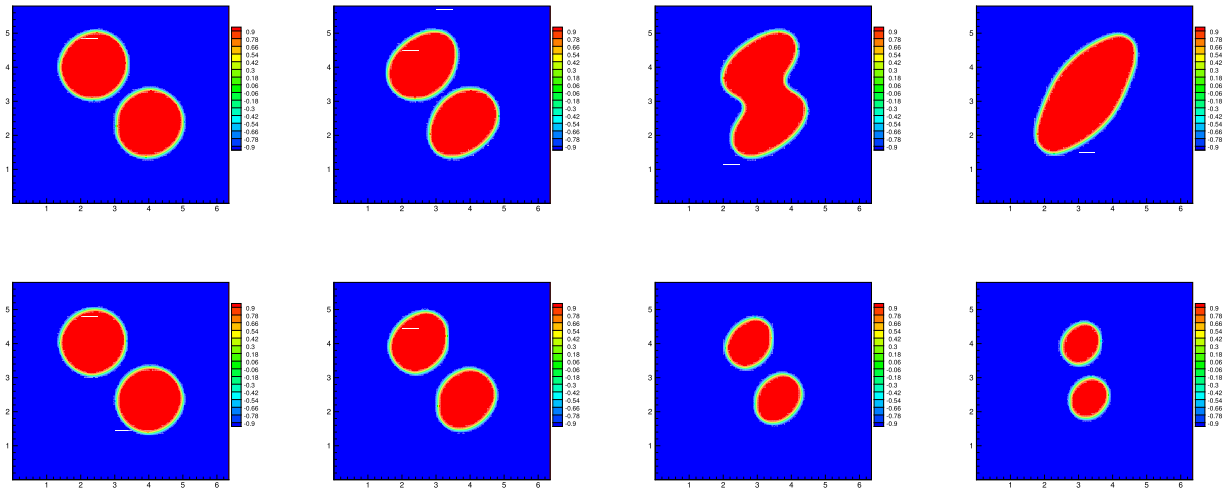

Fig. 11. Snapshots of ϕ with $K = 0$ (first row) and $K = 0.3$ (second row) at different time $t = 1.5$ (first column), $t = 6$ (second column), $t = 15$ (third column) and $t = 25$ (fourth column).

Example 5.5 (Shear flow)**.** In this example, we study the dynamics of two droplets suspended in a shear flow within a square domain $\Omega = [0, 6.4] \times [0, 6.4]$. The initial conditions for the phase-field variable ϕ, the solute concentrations $C_{\pm}$ and velocity $\boldsymbol{u}$ are given by

$$\phi(x, y, 0) = \tanh\left(\frac{1.0 - \sqrt{(x-2.35)^2 + (y-4.05)^2}}{\sqrt{2}\epsilon}\right) + \tanh\left(\frac{1.0 - \sqrt{(x-4.05)^2 + (y-2.35)^2}}{\sqrt{2}\epsilon}\right) + 1.0,$$

$$C_+(x, y, 0) = 0.1 + \exp\left(-\frac{(x-2.35)^2 + (y-4.05)^2}{0.15}\right) + \exp\left(-\frac{(x-4.05)^2 + (y-2.35)^2}{0.15}\right),$$

$$C_-(x, y, 0) = 0.02, \quad \boldsymbol{u} = \boldsymbol{0}.$$

We consider two cases: impermeable interfaces ($K = 0$) and semi-permeable interfaces ($K = 0.3$), while keeping all other parameters identical to those in Example 5.3. The boundary conditions are specified as

$$\nabla\phi \cdot \boldsymbol{n}|_{y=0} = \nabla\phi \cdot \boldsymbol{n}|_{y=6.4} = 0, \quad \phi(0, y, t) = \phi(6.4, y, t),$$
$$\nabla\tilde{\mu}_\phi \cdot \boldsymbol{n}|_{y=0} = \nabla\tilde{\mu}_\phi \cdot \boldsymbol{n}|_{y=6.4} = 0, \quad \tilde{\mu}_\phi(0, y, t) = \tilde{\mu}_\phi(6.4, y, t),$$
$$\nabla C_\pm \cdot \boldsymbol{n}|_{y=0} = \nabla C_\pm \cdot \boldsymbol{n}|_{y=6.4} = 0, \quad C_\pm(0, y, t) = C_\pm(6.4, y, t),$$
$$\boldsymbol{u}|_{y=0} = (-1, 0)^T, \quad \boldsymbol{u}|_{y=6.4} = (1, 0)^T,$$

with periodic boundary conditions applied on the left and right boundaries.

Fig. 11 shows the evolution of the droplet interfaces at various time instances for the two different permeability settings. When $K = 0$, the droplets are impermeable, and their enclosed volume remains constant. Under the shear flow, the two initially separated droplets move closer, eventually coalesce into a single elongated droplet, and rotate with the background flow. In contrast, when $K = 0.3$, the membranes become semi-permeable to water. The imbalance between osmotic and hydrostatic pressures leads to cross-interface water flux, causing the droplets to gradually shrink. As the droplet volume decreases, the spatial extent of each droplet reduces, preventing the two droplets from coming into contact and merging. This behavior highlights how permeability not only affects the rate of deformation but also alters the qualitative topological outcome. The osmotic shrinkage prevents contact in a given time window under shear flow due to volume reduction induced by osmotic regulation.

6. Conclusions

In this work, we developed a thermodynamically consistent phase-field model for simulating water transport across semi-permeable interfaces driven by osmotic pressure and hydrostatic pressure differences. Our formulation extends the classical Cahn-Hilliard-Navier-Stokes (CHNS) system by incorporating a cross-interface water flux governed by solute gradients and membrane permeability. This extension leads to a highly nonlinear permeating CHNS model (pCHNS) where volume changes induced by osmotic flow dynamically feed back into the solute distribution, resulting in a tightly coupled and highly nonlinear interaction between fluid motion, interfacial dynamics, and solute transport. A key feature of the model is that the transmembrane solvent flux is inherently bidirectional: depending on the instantaneous balance between osmotic and hydrostatic/mechanical effects near the interface, the system may exhibit either swelling or shrinkage. Our asymptotic analysis shows that, as $\epsilon \to 0$ with $\mathcal{M} = M_0\epsilon$, the proposed phase-field model converges to a sharp-interface formulation whose kinematic law, normal stress jump, and solute impermeability conditions coincide with established models.

To address the computational challenges posed by this strongly coupled system, we proposed a suite of energy-stable and high-order numerical schemes. Spatial discretization is performed using the local discontinuous Galerkin (LDG) method, which provides high-order accuracy, nonlinear stability, and flexibility for adaptive mesh refinement. For time integration, we first constructed a first-order decoupled temporal scheme and rigorously proved its unconditional energy stability. To further improve temporal accuracy, we incorporated a semi-implicit spectral deferred correction (SDC) method, achieving high-order convergence in both time and space while preserving the model's thermodynamic consistency. Together, these results provide a robust computational framework for fully coupled fluid–solute–interface transport across semi-permeable membranes.

Our study focuses on a thermodynamically consistent setting to isolate the core mechanisms of osmotic-hydrostatic permeation. For clarity and to enable sharp-interface consistency and energy-stable discretizations, we work in two dimensions with simple droplet geometries, model interfacial mechanics via capillarity, treat the interface as water-permeable and solute-impermeable, and use spatially uniform material parameters. These choices serve exposition and analysis, and the framework is general, so they can be relaxed. In particular, the present work does not yet include more realistic membrane mechanics such as bending elasticity or surface-area constraints, which can nevertheless be incorporated within the same thermodynamically consistent energetic framework [4,13]. Looking ahead, we will incorporate additional biophysics and membrane physics, including ionic transport and electrochemical coupling, bending and inextensibility constraints, surface viscosity, and variable surface tension. We also plan to extend the present framework to fully three-dimensional simulations with adaptive refinement and scalable solvers, and to pursue quantitative comparisons with controlled experiments, such as vesicle swelling/burst cycles, osmotic aspiration, and micropipette tests, together with systematic parameter calibration and sensitivity analysis. Another promising direction is to integrate the present physics-based framework with data-driven methods, including parameter estimation from experiments, uncertainty quantification, and machine-learning-assisted surrogate modeling [40,41]. Such a combination may further enhance the quantitative predictive capability of the model and broaden its applicability to realistic biological and engineering systems.

Declaration of generative AI and AI-assisted technologies in the writing process

During the preparation of this work, the authors used ChatGPT to improve the language and readability. After using this tool/service, the author(s) reviewed and edited the content as needed and take(s) full responsibility for the content of the published article.

CRediT authorship contribution statement

Ruihan Guo: Writing – review & editing, Writing – original draft, Visualization, Validation, Methodology, Funding acquisition, Formal analysis, Conceptualization; **Jie Shen:** Writing – review & editing, Methodology, Conceptualization; **Shixin Xu:** Writing – review & editing, Writing – original draft, Validation, Supervision, Methodology, Funding acquisition, Formal analysis, Conceptualization; **Xianmin Xu:** Writing – review & editing, Writing – original draft, Methodology, Formal analysis, Conceptualization.

Data availability

Data will be made available on request.

Declaration of competing interest

The authors declare that they have no known competing financial interests or personal relationships that could have appeared to influence the work reported in this paper.

Acknowledgment

The research reported in this article was partially supported by the National Natural Science Foundation of China under grants nos. 12271492 (R. Guo and S. Xu), 12531015 (J. Shen), 12371415 (X. Xu), 12461160275 (X. Xu), and W2431008 (J. Shen); by the Natural Science Foundation of Henan Province, China, under grant no. 252300421210 (R. Guo); and by the Beijing Natural Science Foundation under grant no. Z240001 (X. Xu); and by the DKU Summer Research Program grant no. 25AKUG0241 (S. Xu) .

Appendix A. Model derivation details

We calculate the time derivative of the total energy given in (2). For the first term, by using the first two equations of Eq. (1), we have

$$\begin{aligned} I_1 &= \frac{d}{dt}\left(\frac{1}{2}\int_\Omega \rho|\boldsymbol{u}|^2 d\boldsymbol{x}\right) \\ &= \frac{1}{2}\int_\Omega \frac{\partial \rho}{\partial t}|\boldsymbol{u}|^2 d\boldsymbol{x} + \int_\Omega \rho \boldsymbol{u}\cdot\frac{\partial \boldsymbol{u}}{\partial t} d\boldsymbol{x} \\ &= \frac{1}{2}\int_\Omega \frac{\partial \rho}{\partial t}|\boldsymbol{u}|^2 d\boldsymbol{x} + \int_\Omega \rho \boldsymbol{u}\cdot\frac{\mathbf{D}\boldsymbol{u}}{\mathbf{D}t} d\boldsymbol{x} + \int_\Omega \nabla\cdot(\rho\boldsymbol{u})\frac{|\boldsymbol{u}|^2}{2} d\boldsymbol{x} \end{aligned}$$

$$
\begin{aligned}
&= \int_\Omega \boldsymbol{u}\cdot(\nabla\cdot\boldsymbol{\sigma}_\eta + \nabla\cdot\boldsymbol{\sigma}_\phi)d\boldsymbol{x} - \int_\Omega p\nabla\cdot\boldsymbol{u}d\boldsymbol{x}\\
&= -\int_\Omega \nabla\boldsymbol{u} : (\boldsymbol{\sigma}_\eta + \boldsymbol{\sigma}_\phi)d\boldsymbol{x} - \int_\Omega p\nabla\cdot\boldsymbol{u}d\boldsymbol{x}.
\end{aligned} \tag{84}
$$

where pressure is induced as a Lagrange multiplier for incompressibility.

For the second term, the equation of the concentrations and label functions yields

$$
\begin{aligned}
I_2 + I_3 &= \frac{d}{dt}\left\{\int_\Omega RT\left(\zeta_+C_+(\ln\frac{C_+}{c_\infty}-1)+\zeta_-C_-(\ln\frac{C_-}{c_\infty}-1)\right)d\boldsymbol{x} + \int_\Omega\lambda\left(\frac{l^2|\nabla\phi|^2}{2}+F(\phi)\right)d\boldsymbol{x}\right\}\\
&= \int_\Omega RT\left(\zeta_+\ln\frac{C_+}{c_\infty}\frac{\partial C_+}{\partial t}+\zeta_-\ln\frac{C_+}{c_\infty}\frac{\partial C_-}{\partial t}\right)d\boldsymbol{x}\\
&\quad+\int_\Omega\left(RT\left(\frac{\partial\zeta_+}{\partial\phi}C_+(\ln\frac{C_+}{c_\infty}-1)+\frac{\partial\zeta_-}{\partial\phi}C_-(\ln\frac{C_-}{c_\infty}-1)\right)+\mu_\phi\right)\frac{\partial\phi}{\partial t}d\boldsymbol{x}\\
&= \int_\Omega RT\left(\ln\frac{C_+}{c_\infty}\frac{\partial(\zeta_+C_+)}{\partial t}+\ln\frac{C_+}{c_\infty}\frac{(\partial\zeta_-C_-)}{\partial t}\right)d\boldsymbol{x}\\
&\quad+\int_\Omega\left(RT\left(\frac{\partial\zeta_+}{\partial\phi}C_+(\ln\frac{C_+}{c_\infty}-1)+\frac{\partial\zeta_-}{\partial\phi}C_-(\ln\frac{C_-}{c_\infty}-1)\right)+\mu_\phi - C_+\ln\frac{C_+}{c_\infty}\frac{\partial\zeta_+}{\partial\phi}-C_-\ln\frac{C_-}{c_\infty}\frac{\partial\zeta_-}{\partial\phi}\right)\frac{\partial\phi}{\partial t}d\boldsymbol{x}\\
&= \int_\Omega RT\left(\ln\frac{C_+}{c_\infty}\frac{\partial(\zeta_+C_+)}{\partial t}+\ln\frac{C_+}{c_\infty}\frac{\partial(\zeta_-C_-)}{\partial t}\right)d\boldsymbol{x}+\int_\Omega\left(RT\left(-\frac{\partial\zeta_+}{\partial\phi}C_+-\frac{\partial\zeta_-}{\partial\phi}C_-\right)+\mu_\phi\right)\frac{\partial\phi}{\partial t}d\boldsymbol{x}\\
&= \int_\Omega RT\left(-\ln\frac{C_+}{c_\infty}\nabla\cdot(\zeta_+C_+\boldsymbol{u})-\ln\frac{C_+}{c_\infty}\nabla\cdot(\zeta_-C_-\boldsymbol{u})\right)d\boldsymbol{x}\\
&\quad+\int_\Omega RT\left(-\ln\frac{C_+}{c_\infty}\nabla\cdot(\zeta_+\boldsymbol{J}_+)-\ln\frac{C_-}{c_\infty}\nabla\cdot(\zeta_-\boldsymbol{J}_-)\right)d\boldsymbol{x}\\
&\quad+\int_\Omega\tilde{\mu}_\phi(-\nabla\cdot(\boldsymbol{u}\phi)-\nabla\cdot\boldsymbol{J}_\phi+S_\phi|\nabla\phi|)d\boldsymbol{x}\\
&= \int_\Omega(RT\zeta_+\nabla C_+\cdot\boldsymbol{u}+RT\zeta_-\nabla C_-\cdot\boldsymbol{u})d\boldsymbol{x}+\int_\Omega(\zeta_+\boldsymbol{J}_+\cdot\nabla\mu_c^+ +\zeta_-\boldsymbol{J}_-\cdot\nabla\mu_c^-)d\boldsymbol{x}\\
&\quad+\int_\Omega(\nabla\tilde{\mu}_\phi\phi\cdot\boldsymbol{u}+\boldsymbol{J}_\phi\cdot\nabla\tilde{\mu}_\phi)d\boldsymbol{x}+\int_\Omega\tilde{\mu}_\phi S_\phi|\nabla\phi|d\boldsymbol{x}\\
&= \int_\Omega(RT\zeta_+\nabla C_+ + RT\zeta_-\nabla C_- + \nabla\tilde{\mu}_\phi\phi)\cdot\boldsymbol{u}d\boldsymbol{x}\\
&\quad+\int_\Omega(\zeta_+\boldsymbol{J}_+\cdot\nabla\mu_c^+ +\zeta_-\boldsymbol{J}_-\cdot\nabla\mu_c^-)d\boldsymbol{x}+\int_\Omega\boldsymbol{J}_\phi\cdot\nabla\tilde{\mu}_\phi d\boldsymbol{x}+\int_\Omega\tilde{\mu}_\phi S_\phi|\nabla\phi|d\boldsymbol{x}\\
&= \int_\Omega(-(RT\frac{\partial\zeta_+}{\partial\phi}C_+ + RT\frac{\partial\zeta_-}{\partial\phi}C_-)-\tilde{\mu}_\phi)\nabla\phi\cdot\boldsymbol{u}d\boldsymbol{x}+\int_\Omega(\zeta_+\boldsymbol{J}_+\cdot\nabla\mu_c^+ +\zeta_-\boldsymbol{J}_-\cdot\nabla\mu_c^-)d\boldsymbol{x}\\
&\quad+\int_\Omega\boldsymbol{J}_\phi\cdot\nabla\tilde{\mu}_\phi dx+\int_\Omega\tilde{\mu}_\phi S_\phi|\nabla\phi|d\boldsymbol{x}\\
&= -\int_\Omega\mu_\phi\nabla\phi\cdot\boldsymbol{u}d\boldsymbol{x}+\int_\Omega(\zeta_+\boldsymbol{J}_+\cdot\nabla\mu_c^+ +\zeta_-\boldsymbol{J}_-\cdot\nabla\mu_c^-)d\boldsymbol{x}\\
&\quad+\int_\Omega\boldsymbol{J}_\phi\cdot\nabla\tilde{\mu}_\phi d\boldsymbol{x}+\int_\Omega\tilde{\mu}_\phi S_\phi|\nabla\phi|d\boldsymbol{x}\\
&= \int_\Omega -\lambda l^2(\nabla\phi\otimes\nabla\phi):\nabla\boldsymbol{u}d\boldsymbol{x}+\int_\Omega(\zeta_+\boldsymbol{J}_+\cdot\nabla\mu_c^+ +\zeta_-\boldsymbol{J}_-\cdot\nabla\mu_c^-)d\boldsymbol{x}+\int_\Omega\boldsymbol{J}_\phi\cdot\nabla\tilde{\mu}_\phi d\boldsymbol{x}+\int_\Omega\tilde{\mu}_\phi S_\phi|\nabla\phi|d\boldsymbol{x}
\end{aligned} \tag{85}
$$

In summary, we have

$$
\begin{aligned}
&\frac{dE}{dt}\\
&= -\int_\Omega\nabla\boldsymbol{u}:(\boldsymbol{\sigma}_\eta+\boldsymbol{\sigma}_\phi)d\boldsymbol{x}-\int_\Omega p\nabla\cdot\boldsymbol{u}d\boldsymbol{x}-\int_\Omega\lambda l^2(\nabla\phi\otimes\nabla\phi):\nabla\boldsymbol{u}d\boldsymbol{x}+\int_\Omega(\zeta_+\boldsymbol{J}_+\cdot\nabla\mu_c^+ +\zeta_-\boldsymbol{J}_-\cdot\nabla\mu_c^-)d\boldsymbol{x}\\
&\quad+\int_\Omega\boldsymbol{J}_\phi\cdot\nabla\tilde{\mu}_\phi d\boldsymbol{x}+\int_\Omega\tilde{\mu}_\phi S_\phi|\nabla\phi|d\boldsymbol{x}\\
&= -\Delta.
\end{aligned}
$$

References

[1] X. Gong, Z. Gong, H. Huang, An immersed boundary method for mass transfer across permeable moving interfaces, J. Comput. Phys. 278 (2014) 148–168.
[2] H. Jiang, S.X. Sun, Cellular pressure and volume regulation and implications for cell mechanics, Biophys. J. 105 (3) (2013) 609–619.
[3] E. Delpire, K.B. Gagnon, Water homeostasis and cell volume maintenance and regulation, Curr. Top. Membr. 81 (2018) 3–52.
[4] X. Tang, S. Li, J.S. Lowengrub, S.M. Wise, Phase field modeling and computation of vesicle growth or shrinkage, J. Math. Biol. 86 (6) (2023) 97.

[5] S.N. Ho, Intracellular water homeostasis and the mammalian cellular osmotic stress response, J. Cell. Physiol. 206 (1) (2006) 9–15.
[6] F.A. Amiri, J. Zhang, An immersed membrane method for mass transfer across flexible semipermeable membranes in flows, Int. Commun. Heat Mass Transf. 128 (2021) 105601.
[7] A.T. Layton, Modeling water transport across elastic boundaries using an explicit jump method, SIAM J. Sci. Comput. 28 (6) (2006) 2189–2207.
[8] X. Wang, X. Gong, K. Sugiyama, S. Takagi, H. Huang, An immersed boundary method for mass transfer through porous biomembranes under large deformations, J. Comput. Phys. 413 (2020) 109444.
[9] L. Yao, Y. Mori, A numerical method for osmotic water flow and solute diffusion with deformable membrane boundaries in two spatial dimension, J. Comput. Phys. 350 (2017) 728–746.
[10] D.M. Anderson, G.B. McFadden, A.A. Wheeler, Diffuse-interface methods in fluid mechanics, Annu. Rev. Fluid Mech. 30 (1) (1998) 139–165. https://doi.org/10.1146/annurev.fluid.30.1.139
[11] Q. Du, C. Liu, R. Ryham, X. Wang, Energetic variational approaches in modeling vesicle and fluid interactions, Phys. D 238 (9–10) (2009) 923–930.
[12] J. Lowengrub, L. Truskinovsky, Quasi-incompressible Cah-Hilliard fluids and topological transitions, Proceed. Roy. Soc. Lond. Ser. A: Math., Phys. Eng. Sci. 454 (1978) (1998) 2617–2654. https://doi.org/10.1098/rspa.1998.0273
[13] L. Shen, Z. Xu, P. Lin, H. Huang, S. Xu, An energy stable C^0 finite element scheme for a phase-field model of vesicle motion and deformation, SIAM J. Sci. Comput. 44 (1) (2022) B122–B145.
[14] J. Yang, Y. Li, J. Kim, Totally decoupled implicit–explicit linear scheme with corrected energy dissipation law for the phase-field fluid vesicle model, Comput. Method. Appl. Mech. Eng. 399 (2022) 115330.
[15] X. Hu, X. Song, Q. Xia, J. Kim, Y. Li, An unconditional energy stable numerical scheme for fluid-surfactant system with data assimilation method: X. Hu et al., Comput. Appl. Math. 45 (7) (2026) 273.
[16] A. Rätz, Diffuse-interface approximations of osmosis free boundary problems, SIAM J. Appl. Math. 76 (3) (2016) 910–929.
[17] H. Garcke, K.F. Lam, B. Stinner, Diffuse interface modelling of soluble surfactants in two-phase flow, Commun. Math. Sci. 12 (2013) 1475–1522.
[18] B.A. Camley, Y. Zhao, B. Li, H. Levine, W.-J. Rappel, Periodic migration in a physical model of cells on micropatterns, Phys. Rev. Lett. 111 (15) (2013) 158102.
[19] J. Lowengrub, J. Allard, S. Aland, Numerical simulation of endocytosis: Viscous flow driven by membranes with non-uniformly distributed curvature-inducing molecules, J. Comput. Phys. 309 (2016) 112–128.
[20] B. Eisenberg, Y. Hyon, C. Liu, Energy variational analysis of ions in water and channels: field theory for primitive models of complex ionic fluids, J. Chem. Phys. 133 (10) (2010) 104104.
[21] L. Shen, H. Huang, P. Lin, Z. Song, S. Xu, An energy stable C^0 finite element scheme for a quasi-incompressible phase-field model of moving contact line with variable density, J. Comput. Phys. 405 (2020) 109179.
[22] R. Chen, G. Ji, X. Yang, H. Zhang, Decoupled energy stable schemes for phase-field vesicle membrane model, J. Comput. Phys. 302 (2015) 509–523.
[23] W. Chen, Y. Liu, C. Wang, S. Wise, Convergence analysis of a fully discrete finite difference scheme for the Cahn-Hilliard-Hele-Shaw equation, Math. Comput. 85 (301) (2016) 2231–2257.
[24] K. Cheng, W. Feng, C. Wang, S.M. Wise, An energy stable fourth order finite difference scheme for the Cahn–Hilliard equation, J. Comput. Appl. Math. 362 (2019) 574–595.
[25] A.E. Diegel, S.W. Walker, A finite element method for a phase field model of nematic liquid crystal droplets, Commun. Comput. Phys. 25 (2019) 155–188.
[26] Z. Guo, P. Lin, J.S. Lowengrub, A numerical method for the quasi-incompressible Cahn–Hilliard–Navier–Stokes equations for variable density flows with a discrete energy law, J. Comput. Phys. 276 (2014) 486–507.
[27] Y. Yan, W. Chen, C. Wang, S.M. Wise, A second-order energy stable BDF numerical scheme for the Cahn-Hilliard equation, Commun. Comput. Phys. 23 (2) (2018) 572–602.
[28] X. Yang, G.-D. Zhang, Convergence analysis for the invariant energy quadratization (IEQ) schemes for solving the Cahn–Hilliard and Allen–Cahn equations with general nonlinear potential, J. Sci. Comput. 82 (3) (2020) 1–28.
[29] X. Yang, J. Zhao, Q. Wang, Numerical approximations for the molecular beam epitaxial growth model based on the invariant energy quadratization method, J. Comput. Phys. 333 (2017) 104–127.
[30] R. Guo, Y. Xu, High order numerical simulations for the binary fluid-surfactant system using the discontinuous Galerkin and spectral deferred correction methods, SIAM J. Sci. Comput. 42 (2020) B353–B378.
[31] Y. Xu, C.-W. Shu, Local discontinuous Galerkin methods for high-order time-dependent partial differential equations, Comm. Comput. Phys. 7 (2010) 1–46.
[32] R. Guo, Y. Xia, Arbitrary high-order fully-decoupled numerical schemes for phase-field models of two-phase incompressible flows, Commun. Appl. Math. Comput. 6 (2024) 625–657.
[33] R. Guo, Y. Xu, Y. Xia, Semi-implicit spectral deferred correction methods for highly nonlinear partial differential equations, J. Comput. Phys. 338 (2017) 269–284.
[34] X. Li, J. Lowengrub, A. Rätz, A. Voigt, Solving PDEs in complex geometries: a diffuse domain approach, Commun. Math. Sci. 7 (1) (2009) 81.
[35] Y. Qin, H. Huang, Y. Zhu, C. Liu, S. Xu, A phase field model for mass transport with semi-permeable interfaces, J. Comput. Phys. 464 (2022) 111334.
[36] Q. Du, C. Liu, X. Wang, A phase field approach in the numerical study of the elastic bending energy for vesicle membranes, J. Comput. Phys. 198 (2) (2004) 450–468.
[37] X. Xu, Y. Di, H. Yu, Sharp-interface limits of a phase-field model with a generalized Navier slip boundary condition for moving contact lines, J. Fluid Mech. 849 (2018) 805–833.
[38] C.J. Vogl, M.J. Miksis, S.H. Davis, D. Salac, The effect of glass-forming sugars on vesicle morphology and water distribution during drying, J. Roy. Soc. Interface 11 (99) (2014) 20140646.
[39] L.A. Caffarelli, N.E. Muler, An L^∞ bound for solutions of the Cahn-Hilliard equation, Arch. Ration. Mech. Anal. 133 (2) (1995) 129–144.
[40] X. Song, Q. Xia, J. Kim, Y. Li, An unconditional energy stable data assimilation scheme for Navier-Stokes-Cahn-Hilliard equations with local discretized observed data, Comput. Math. Applic. 164 (2024) 21–33.
[41] K. Buck, R. Temam, Convergence Properties of PINNs for the Navier-Stokes-Cahn-Hilliard System, (2025). arXiv preprint arXiv:2505.07964